Monthly Notices
of the
ROYAL ASTRONOMICAL SOCIETY

MNRAS **494,** 4226–4243 (2020)
Advance Access publication 2020 April 10

doi:10.1093/mnras/staa969

New insight into the stellar mass function of Galactic globular clusters

H. Ebrahimi,[1]★ A. Sollima,[2] H. Haghi,[1] H. Baumgardt[3] and M. Hilker[4]

[1]*Department of Physics, Institute for Advanced Studies in Basic Sciences (IASBS), Zanjan 45137-66731, Iran*
[2]*INAF Osservatorio Astrofisica e Scienza dello Spazio, via Gobetti 93/3, I-Bologna 40129, Italy*
[3]*School of Mathematics and Physics, The University of Queensland, St. Lucia, QLD 4072, Australia*
[4]*European Southern Observatory, Karl-Schwarzschild-Str. 2, D-85748 Garching, Germany*

Accepted 2020 March 31. Received 2020 February 9; in original form 2019 October 24

ABSTRACT

We present the results of the analysis of deep photometric data of 32 Galactic globular clusters. We analysed 69 parallel field images observed with the Wide Field Channel of the Advanced Camera for Surveys of the *Hubble Space Telescope* which complemented the already available photometry from the globular cluster treasury project covering the central regions of these clusters. This unprecedented data set has been used to calculate the relative fraction of stars at different masses (i.e. the present-day mass function) in these clusters by comparing the observed distribution of stars along the cluster main sequence and across the analysed field of view with the prediction of multimass dynamical models. For a subsample of 31 clusters, we were able to obtain also the half-mass radii, mass-to-light ratios, and the mass fraction of dark remnants using available radial velocity information. We found that the majority of globular clusters have single power-law mass functions $F(m) \propto m^{\alpha}$ with slopes $\alpha > -1$ in the mass range $0.2 < m/\mathrm{M}_{\odot} < 0.8$. By exploring the correlations between the structural/dynamical and orbital parameters, we confirm the tight anticorrelation between the mass function slopes and the half-mass relaxation times already reported in previous works, and possible second-order dependence on the cluster metallicity. This might indicate the relative importance of both initial conditions and evolutionary effects on the present-day shape of the mass function.

Key words: methods: numerical – techniques: photometric – techniques: radial velocities – stars: kinematics and dynamics – stars: luminosity function, mass function – globular clusters: general.

1 INTRODUCTION

Globular clusters (GCs) are among the most useful objects to study stellar astrophysics. Consisting of a large number of stars with similar ages and chemical compositions they are valuable to test stellar evolution models. Beside their importance in stellar evolution studies, GCs are the oldest collisional systems such that dynamical drivers (like two-body relaxation) and external tidal field have changed their structures. By comparing observational coordinates in phase-space (projected positions and three-dimensional motions) with theoretical models, one can derive many important parameters of GCs like their masses, mass functions (MFs), and degree of mass segregation.

The present-day structure of GCs depends directly on the mass distribution of stars that extends from the faintest stars at the hydrogen burning limit (with masses around 0.1 $\mathrm{M}_{\odot}$) to massive black holes (with masses larger than 15 $\mathrm{M}_{\odot}$). The shape of the present-day MF is the result of the effect of complex mechanisms of dynamical and stellar evolution from the initial mass function (IMF). The universality of the IMF is a highly debated topic in astrophysics (Bastian, Covey & Meyer 2010; Kroupa et al. 2013). The first attempt to introduce a parametrized IMF as a single power-law function was made by Salpeter (1955) and followed by a lognormal (Miller & Scalo 1979; Chabrier 2003), a multisegment power-law (Kroupa, Tout & Gilmore 1993; Kroupa 2001), and a tapered power-law IMF (de Marchi, Paresce & Portegies Zwart 2005). In recent decades, many studies have tried to fit the above functions to the observed MF of various unevolved groups of stars, e.g. field stars (Czekaj et al. 2014; Rybizki & Just 2015; Mor et al. 2019; Sollima 2019), young and embedded clusters (Weights et al. 2009; Weisz et al. 2013), OB associations (Massey 2003; Da Rio et al. 2012), open clusters (Moraux et al. 2003; Sheikhi et al. 2016), and dwarf galaxies (Cappellari et al. 2006; Gennaro et al. 2018). Most studies of resolved stellar populations in the disc of the Milky Way showed that stars form following an IMF that has a universal form (Kroupa 2001, 2002) which is referred to as the 'canonical' IMF. This poses a problem for star formation theories which predict a dependence on the environment where star formation takes place (Kroupa et al. 2013; Chabrier, Hennebelle & Charlot 2014). In spite of no evidence

★ E-mail: h.ebrahimi@iasbs.ac.ir

of significant variations of the IMF in these studies, the universality of the IMF is still a matter of debate. In particular, recent integrated light spectroscopic studies in the centres of giant ellipticals seem to favour a bottom-heavy IMF (Conroy, van Dokkum & Villaume 2017; van Dokkum et al. 2017), while some extragalactic super starburst regions indicate a top-heavy IMF (Zhang et al. 2018).

From the IMF to the present-day MF, the evolution of GC MFs depends on many processes. At early stages, stellar evolution leads to the disruption of the most massive stars depriving the high-mass tail of the IMF. On long time-scale, gravitational encounters among the stars and the interaction of the GC with the external tidal field also alter the shape of the MF. The tendency towards kinetic energy equipartition leads high-mass stars to sink into the core and low-mass stars to migrate towards the outskirts (Spitzer 1987). Low-mass stars can gain enough energy to escape from the GC more efficiently than high-mass ones, with a consequent depletion of the low-mass end of the MF (Lamers, Baumgardt & Gieles 2013). As a result, as the GC loses a significant fraction of its low-mass stars, the faint end of its IMF evolves from its initial towards a flatter shape (Baumgardt & Makino 2003). This process is enhanced by the tidal force exerted by the host galaxy which accelerates the process of mass loss (Gieles, Heggie & Zhao 2011). This so-called 'dynamical' mass segregation might be accompanied by a 'primordial' mass segregation. The evidence and effect of this latter kind of mass segregation has been widely discussed on the basis of both observational (Frank, Grebel & Küpper 2014) and theoretical grounds (Haghi et al. 2014, 2015). For instance, Zonoozi et al. (2011, 2014, 2017) have shown that to explain the MF flattening in the centres of Pal 4 and Pal 14, the presence of both types of mass segregation is necessary. The effect of the various drivers on the evolution of GC MFs has been considered by many studies including many further ingredients, e.g. Galactic disc/bulge shocking (Ostriker, Spitzer & Chevalier 1972; Aguilar, Hut & Ostriker 1988), binary star evolution and interaction (Schneider et al. 2015), and orbital eccentricity (Madrid, Hurley & Martig 2014; Webb et al. 2014).

The proper modelling of mass segregation as a function of radius is crucial to estimate the global MF of a star cluster. Indeed, observations are often localized in a restricted portion of the GC, and suitable corrections are necessary to account for such MF variations (Paust et al. 2010).

From a theoretical perspective, there are a few methods to investigate the dynamical evolution of gravitational systems: *N*-body simulations (Baumgardt & Makino 2003; Webb & Leigh 2015), Fokker–Planck models (Takahashi & Lee 2000; Murphy, Cohn & Lugger 2011), Monte Carlo models (Giersz 2001; Joshi, Nave & Rasio 2001), and through analytic methods (e.g. like the EMACSS code; Alexander et al. 2014). All these models have been used to study the mechanisms driving the evolution from the IMF to the present-day MF.

During the last decades, the *Hubble Space Telescope* (*HST*) has allowed us an unprecedented insight into the GC stellar populations. Within the *HST Treasury program*, Sarajedini et al. (2007) performed uniform photometry of stars in the central region of 65 GCs sampling stars as faint as 0.2 $M_\odot$ with an S/N $\gtrsim$ 10. This program has served many studies aimed at testing stellar evolution, isochrones, luminosity functions, and synthetic horizontal-branch models (Dotter et al. 2007), also deriving the ages of ∼60 GCs (Marín-Franch et al. 2009; Dotter et al. 2010) and the MF of a sample of 17 GCs (Paust et al. 2010). Moreover, the *HST UV legacy survey of Galactic GC program* designed to find multiple stellar populations extended the observational data sets to ultraviolet wavelengths (Piotto et al. 2015; Milone et al. 2017). In the context of this project, Simioni et al. (2018) presented a photometric catalogue of 110 parallel fields in the outskirts of 48 Galactic GCs. By combining the catalogues of the two above mentioned programs, the photometric catalogues of 56 Galactic GCs have been made public (Nardiello et al. 2018). The second data release (DR2) of the *Gaia* mission has also improved the observational scenario of GCs. Among the recent works based on *Gaia* DR2, Baumgardt et al. (2019) have derived the mean proper motions and space velocities of 154 Galactic GCs and the velocity dispersion profiles of 141 GCs.

By comparing observational data and simple dynamical models, several studies have attempted to calculate GC MFs and evaluate possible correlations between GC parameters. Among the most comprehensive studies, but based on heterogeneous measurements, Capaccioli, Piotto & Stiavelli (1993) and Djorgovski, Piotto & Capaccioli (1993) reported a dependence of the MF slopes on the Galactocentric distances and on the heights above the Galactic plane. Piotto & Zoccali (1999) analysed deep *HST* images taken near the half-mass radii of seven GCs and found that the MF slopes correlate with the orbital destruction rates of the clusters and anticorrelate with their half-mass relaxation times, although their small sample hampered any firm conclusion on the significance of these correlations. de Marchi, Paresce & Pulone (2007) derived the MF of 20 GCs using *HST* and Very Large Telescope (VLT) data, reporting a well-defined correlation between the slope of their MFs and their King model concentration parameter *c*. Paust et al. (2010) provided the MF for 17 GCs comparing the luminosity function derived from the *HST Treasury program* data and multimass models and found that the MF slope correlates with central density, but with neither metallicity nor Galactic location. Using to the same data set and a similar technique, Sollima & Baumgardt (2017, hereafter SB17) expanded the sample to 35 GCs. They determined the structural and dynamical parameters of 29 GCs with available radial velocity information and revealed a tight anticorrelation between MF slopes and half-mass relaxation times and correlation with the dark remnant fractions. They concluded that the internal dynamical evolution is the main responsible in shaping the present-day MFs. These last works, while representing the most complete census of MF based on the deepest photometric data set available so far, suffer from the lack of information outside the GC cores and constrain the model predictions only with the MF measured in the cluster centre. This can potentially lead to significant bias in the estimated MF, in particular in those GCs whose extent exceeds the field of view of the available data (Sollima et al. 2015). By fitting a large set of *N*-body simulations to their velocity dispersion and surface density profiles, the correlation between MF slope and relaxation time has been confirmed by Baumgardt & Hilker (2018, hereafter BH18).

In this paper, we present the results of the photometric analysis of 69 *HST*/ACS/WFC parallel fields for 32 Galactic GCs and combine them with the available data from the *HST Treasury program* in the central regions of these GCs. This unprecedented data set is used to derive the global present-day MFs through the comparison with multimass analytical models.

This paper is organized as follows: in Section 2 the observational material is presented and the data reduction technique is described. The multimass dynamical model, the algorithm of MF determination, and fitting technique are described in Sections 3 and 4. In Section 5 we present the derived GCs' MF and look for the possible correlations with various parameters. We summarize our results in Section 6.

2 PHOTOMETRY AND DATA REDUCTION

Images have been obtained with the Advanced Camera for Surveys (ACS) onboard *HST* using the single channel camera WFC. The detector includes two similar chips of 2048 × 4096 pixels each with a pixel-scale of 0.05 arcsec per pixel. Therefore the entire channel covers an effective field of view of 202 arcsec × 202 arcsec. The photometric catalogues in the F606W and F814W filters of the region around the centres of 65 GCs have been published as part of the *HST Treasury program* (Sarajedini et al. 2007). The results of artificial star experiment performed on this data set have been also provided by Anderson et al. (2008).

Parallel pointings for all the GCs included in the *HST Treasury project* are also available as ancillary products of the *HST UV legacy survey of Galactic GCs program*. In a recent work, Simioni et al. (2018) provided accurate photometry for these pointings together with cluster membership probabilities. Unfortunately, no artificial star experiments (essential for our purpose to estimate the catalogue completeness at different magnitudes and in different crowding conditions) were performed by these authors. So, we performed an independent photometric analysis of this data set and the artificial star experiments consistently. Among the entire sample of GCs included in the *HST Treasury project*, we excluded NGC 4147 and NGC 6205 because of the lack of parallel field images available until 2018. After performing the photometric process, we exclude some further GCs because of (i) contamination by the Sagittarius stream (e.g. NGC 6652 and NGC 6681) or the Sagittarius dwarf galaxy (e.g. NGC 6715) or the bulge (e.g. NGC 6624 and NGC 6637), (ii) large helium variation ($\Delta Y > 0.1$; e.g. NGC 2808, NGC 5139, NGC 6388, and NGC 6441) affecting the mass–luminosity relation along the main sequence, and (iii) a completeness level below 10 per cent at the hydrogen-burning limit (e.g. NGC 6171, NGC 6934, and NGC 6981). A final sample of 32 GCs passed the above criteria (see Table 1).

We retrieved images of 69 parallel fields (pointings) in the outer region of these 32 GCs provided by the *HST*/ACS/WFC public archive and released before 2018. These pointings are centred approximately from 6 to 12 arcmin from the centre of the target GCs. In Fig. 1, the maps of the region sampled by those observations are shown. Each pointing consists of several images differing from each other because of their different filters and exposure times. We selected them in order to ensure at least two images observed through two different filters (including F814W) and with an exposure time long enough to allow to construct a deep colour–magnitude diagram (CMD) sampling star with masses down to ∼0.15 $M_{\odot}$. In our collected samples, each parallel pointing has only one filter pair: (F606W, F814W) or (F475W, F814W). All GCs with multiple parallel pointings (with the exception of NGC 104) have been observed with the same filter pair. For simplicity, in spite of their different throughput, we will name the F475W/F606W magnitudes as V magnitude and the F814W magnitude as I magnitude. The logs of the observations are listed in Table 1.

We performed the photometric analysis on the flat-fielded *HST*/ACS/WFC images corrected for the charge-transfer efficiency (`flc`) while the drizzled (`drc`) images were used for source detection. We employed the stellar photometry package DOLPHOT v2 optimized in the HSTPHOT extension (Dolphin 2000) to analyse ACS images (Dolphin 2016). A high signal-to-noise (S/N) image has been created by aligning and stacking all available `drc` images of each pointing and used to create a list of detected sources. This reference image has then been used as input by the DOLPHOT

Table 1. Observing logs.

NGC	Pointing	Filter	Exposure time (s)
104	1	F475W	1050; 2 × 986; 947; 2 × 880
		F814W	877; 870; 806; 800; 767; 760
	2	F606W	1498; 1457; 1443
			1442; 1385; 1371
		F814W	1457;1371; 1358; 1357
			1303; 1118; 100
288	1	F606W	3 × 200; 15
		F814W	3 × 150; 10
362	1	F606W	172; 86; 39
		F814W	60; 25
1261	1	F475W	770
		F814W	694
	2	F475W	745
		F814W	669
	3	F475W	766
		F814W	690
	4	F475W	745
		F814W	669
	5	F475W	829
		F814W	753
1851	1	F475W	2 × 1277; 1237; 2 × 40
		F814W	6 × 488; 40
	2	F475W	2 × 1277; 2 × 1237; 2 × 40
		F814W	8 × 488; 2 × 40
2298	1	F475W	2 × 785
		F814W	2 × 683
	2	F475W	887; 885
		F814W	816; 815
3201	1	F475W	685
		F814W	612
	2	F475W	689
		F814W	616
4590	1	F475W	627
		F814W	554
	2	F475W	627
		F814W	554
5024	1	F475W	4 × 725; 2 × 723
		F814W	3 × 370
	2	F475W	4 × 775; 2 × 774
		F814W	3 × 375
5053	1	F475W	740
		F814W	664
	2	F475W	740
		F814W	664
	3	F475W	790
		F814W	714
	4	F475W	790
		F814W	714
	5	F475W	765
		F814W	689
5272	1	F475W	3 × 800
		F814W	3 × 760
5286	1	F475W	728
		F814W	655
	2	F475W	603
		F814W	559

Table 1 – *continued*

NGC	Pointing	Filter	Exposure time (s)
5466	1	F475W	835; 834
		F814W	765; 763
	2	F475W	2 × 776
		F814W	2 × 700
5897	1	F475W	833; 830
		F814W	2 × 761
	2	F475W	781; 779
		F814W	710; 709
5904	1	F475W	620
		F814W	559
	2	F475W	621
		F814W	559
5986	1	F475W	676
		F814W	603
	2	F475W	2 × 603
		F814W	2 × 559
6093	1	F475W	5 × 845; 5 × 760
		F814W	5 × 539
6101	1	F475W	762
		F814W	686
	2	F475W	762
		F814W	686
	3	F475W	800
		F814W	724
	4	F475W	851
		F814W	775
	5	F475W	800
		F814W	724
6144	1	F475W	679
		F814W	606
	2	F475W	679
		F814W	606
6218	1	F475W	721
		F814W	648
	2	F475W	645
		F814W	572
6254	1	F475W	721
		F814W	648
	2	F475W	644
		F814W	571
6341	1	F475W	638
		F814W	565
	2	F475W	750
		F814W	677
6362	1	F475W	651
		F814W	578
	2	F475W	760
		F814W	687
6541	1	F475W	689
		F814W	616
	2	F475W	639
		F814W	566
6584	1	F475W	640
		F814W	567
	2	F475W	726
		F814W	653

Table 1 – *continued*

NGC	Pointing	Filter	Exposure time (s)
6723	1	F475W	666
		F814W	592
	2	F475W	626
		F814W	551
	3	F475W	624
		F814W	551
6752	1	F606W	500
		F814W	200; 15
6779	1	F475W	731
		F814W	658
	2	F475W	637
		F814W	564
6809	1	F475W	753
		F814W	680
	2	F475W	677
		F814W	604
7078	1	F475W	4 × 702
		F814W	4 × 121
7089	1	F475W	717
		F814W	643
	2	F475W	668
		F814W	593
	3	F475W	611
		F814W	534
7099	1	F475W	656
		F814W	583
	2	F475W	656
		F814W	583

point spread function (PSF)-fitting routine which has been run on individual images. Aperture corrections have been computed using the most isolated and bright sources and applied to the output catalogue. In this catalogue, the average magnitude of each detected star and those measured in all the individual `flc` images were listed together with quality flags, S/N, roundness, sharpness, and star positions in pixels. To select an optimal set of stars, we set the following criteria: (i) at least two reasonable magnitudes should exist per filter for each star in each pointing, (ii) an absolute value of sharpness smaller than 0.1;[1] (iii) an object type flag equal to 1, which corresponds to good stars; (iv) a photometry quality flag less than 4, which includes stars with negligible photometric errors. We cross-correlated our catalogues with those provided by Simioni et al. (2018) to convert (x,y) coordinates into the standard astrometric reference system (*RA*, *Dec.*). A star-by-star comparison between our photometry and that of Simioni et al. (2018) indicates average differences between the two data sets of ΔV, ΔI (this work–Simioni et al.) = 0.04 in V and I passbands for all the GCs of the sample, indicating a small shift in the calibration process. The CMDs of the central region and of the parallel fields of NGC 104 and NGC 288 are shown in Fig. 2.[2]

[1]This criterion came from the definition of sharpness (Dolphin 2000): the sharpness of completely flat, sharp, and perfectly fit stars are −1, 1, and 0, respectively.

[2]The CMDs of the other GCs are available as Supporting Information in the online version of the paper.

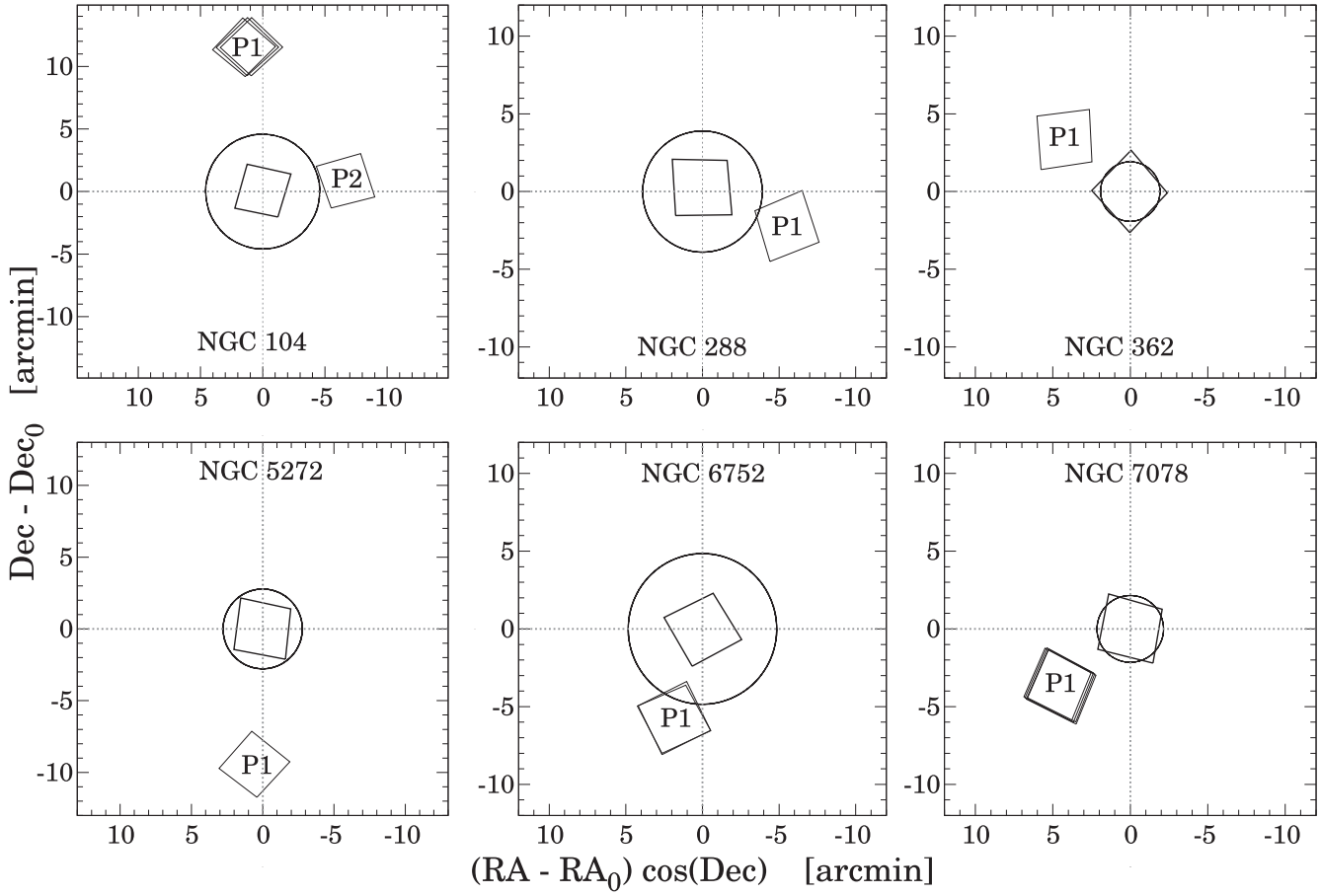

Figure 1. Maps of the pointings around the six GCs analysed here and not present in the Simioni et al. (2018) sample. The squares in the centre show the regions covered by the *HST* Treasury program. The squares labelled by 'P' mark the location of the parallel pointings. The half-mass radii (from this work) are marked with circles. The maps of the other GCs of our sample are available in Simioni et al. (2018).

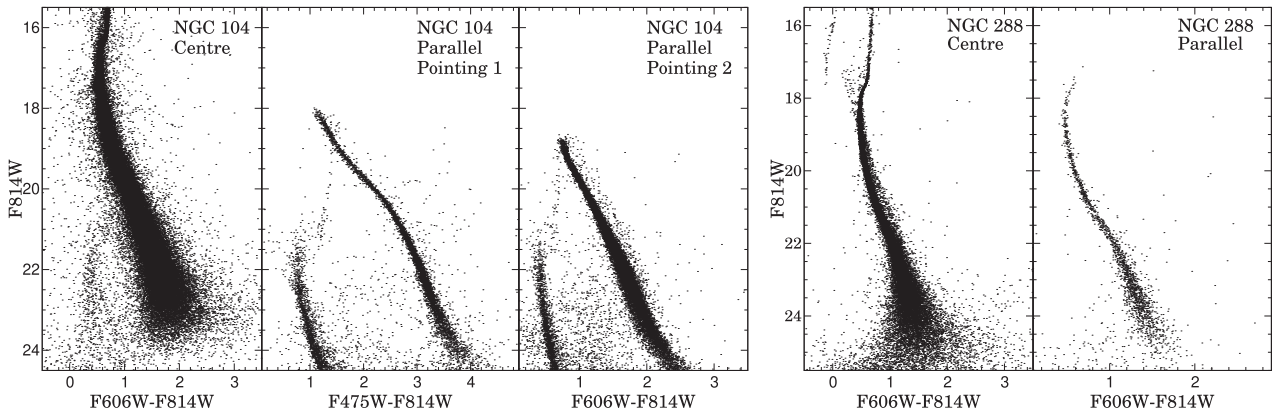

Figure 2. CMD of NGC 104 (left-hand panels) and NGC 288 (right-hand panels). The same plot for the entire sample of GCs is available as Supporting Information in the online version of the paper.

To perform artificial star experiments for a pointing in each GC, an input set of fake stars has been simulated. The positions of fake stars have been chosen by defining a regular grid of 190 × 190 cells separated by 20 pixels in each direction, which cover homogeneously the ACS/WFC field of view. Artificial stars have been placed at a random position within a 16 × 16 pixel square centred around each grid knot (one star per cell). Given the typical size of the ACS/WFC PSF (*FWHM* ∼ 2 px) this ensures that artificial stars cannot blend each other (self-crowding). The magnitudes of stars have been extracted from the theoretical isochrone provided by Dotter et al. (2007) with the suitable age, metallicity, and alpha-element abundance of each GC (Dotter et al. 2010). The absolute magnitudes of stars have been converted into the apparent ones by adopting the distance moduli and reddening determined by Dotter

et al. (2010). The masses of fake stars were extracted from a Kroupa IMF (Kroupa 2001) covering the full range of masses covered by the isochrone from the hydrogen burning limit up to the red giant branch tip. The corresponding magnitudes of fake stars have been used by DOLPHOT to normalize the fluxes of the PSF which have been placed into the original science images and the photometric analysis has then been performed on synthetic images with the same prescriptions adopted for the original frames. With the above procedure, 36 100 fake stars have been simulated per run. Moreover, several (from 1 to 5, depending on the number of GC pointings) independent runs have been performed in each GC and the artificial star catalogues of different runs have been stacked together in a unique list containing from 36 100 to 180 500 artificial stars. An artificial star has been considered as recovered if the difference between its input and output magnitudes is smaller than 2.5log (2) ~ 0.752 mag in both V and I magnitudes.

For a subsample of 31 GCs we were able to derive the dynamical parameters through the comparison with the set of available radial velocities. For this purpose we used the sample of radial velocities derived by BH18[3] which have been obtained from a combination of more than 45 000 high-resolution spectra observed with FLAMES@VLT and DEIMOS@Keck stars with literature data. For the 31 GCs in our sample, the number of stars with available radial velocities ranges from 19 (for the lowest mass GC NGC 6144) to 2867 (for the most massive GC NGC 104).

3 MODELS

To convert the relative distribution of stars at different radii into the global MF, a suitable dynamical model is needed. The structure of multimass stellar systems can be obtained from the phase-space distribution of stars proposed by Michie (1963) and King (1966). The isotropic form of this distribution is (Gunn & Griffin 1979):

$$f(E) = \sum_{i=1}^{H} k_i f(m_i, r, v) = \sum_{i=1}^{H} k_i \left[\exp\left(\frac{-A_i E}{\sigma_K^2} \right) - 1 \right], \quad (1)$$

where H is the number of mass components, m_i is the mass of the ith component, v and r are the 3D velocity and distance from the GC centre, k_i are coefficients determining the number of stars in each mass bin, A_i are coefficients regulating the equilibrium among the stars with different masses, and σ_K^2 is a constant determining the normalization in energy. $E = v^2/2 + \psi(r)$ is the energy per unit mass, where ψ is the effective potential defined as the difference between the potential at an arbitrary radius and the potential at the GC tidal radius, r_t. Following Gunn & Griffin (1979), we adopted $A_i \propto m_i$. A degree of radial anisotropy can be accounted for by multiplying the above distribution function by a term depending on the angular momentum. Watkins et al. (2015) analysed the *HST* proper motions of a sample of 22 nearby GCs and showed that deviations from isotropy are negligible within GC cores and only a mild anisotropic velocity distributions near the half-mass radius is detectable. Thus, to limit the number of free parameters, we adopted the isotropic form of the distribution functions (equation 1).

By integrating the distribution function over v and r, the 3D number density, velocity dispersion, number of stars, projected number density, and line-of-sight velocity dispersion can be derived for each mass group respectively as

$$n_i(r) = \int_0^{\sqrt{-2\psi(r)}} 4\pi v^2 k_i f(m_i, r, v)\, \mathrm{d}v, \quad (2)$$

$$\sigma_{v,i}^2(r) = \frac{1}{n_i(r)} \int_0^{\sqrt{-2\psi(r)}} 4\pi v^4 k_i f(m_i, r, v)\, \mathrm{d}v, \quad (3)$$

$$N_i = \int_0^{r_t} 4\pi r^2 n_i(r)\, \mathrm{d}r, \quad (4)$$

$$\Gamma(m_i, R) = 2 \int_R^{r_t} \frac{r n_i(r)}{\sqrt{r^2 - R^2}}\, \mathrm{d}r, \quad (5)$$

$$\sigma_{\mathrm{LOS},i}^2(R) = \frac{2}{3\Gamma_i(R)} \int_R^{r_t} \frac{r n_i(r) \sigma_{v,i}^2(r)}{\sqrt{r^2 - R^2}}\, \mathrm{d}r, \quad (6)$$

while the mean mass is given by

$$\bar{m} = \frac{\sum_{i=1}^{H} N_i m_i}{\sum_{i=1}^{H} N_i}. \quad (7)$$

The radial gradient of $\psi(r)$ is given by the Poisson equation as:

$$\nabla^2 \psi(r) = 4\pi G \rho(r), \quad (8)$$

while the global 3D density is determined by the following expression:

$$\rho(r) = \sum_{i=1}^{H} m_i n_i(r). \quad (9)$$

To integrate the above equations, appropriate boundary conditions need to be set. At the centre the value of the potential ($W_0 \equiv -\psi_0/\sigma_k^2$) has been left as a free parameter while its derivative has been set to $\mathrm{d}\psi/\mathrm{d}r(0) = 0$. At the tidal radius, defined as the distance where both density and potential vanish, we set $\psi(r_t) = 0$.

Along with k_i, two additional free parameters complete the definition of the models: $r_c \equiv \sqrt{9\sigma_k^2/4\pi G\rho_0}$ and σ_k^2 which determine the size and mass of the system. The total mass, luminosity, and surface brightness profile can be obtained respectively as

$$M = \sum_{i=1}^{H} N_i m_i, \quad (10)$$

$$L_V = \sum_{i=1}^{H} N_i \mathcal{F}_i, \quad (11)$$

$$\mu = -2.5 \log \left(\sum_{i=1}^{H} \Gamma_i \mathcal{F}_i \right), \quad (12)$$

where $\mathcal{F}_i$ is the average V-band flux of stars in the ith component.

4 METHOD

Sollima, Bellazzini & Lee (2012), Sollima et al. (2017), and SB17 have described a method to determine the global GCs MF and the structural/dynamical parameters of GCs and we adopt their method in this paper.

Briefly, an iterative procedure has been implemented. At each iteration, a guess of the MF and of the model parameters is chosen and a synthetic population of particles with the corresponding masses (magnitudes) and radial distributions has been simulated. The effect of completeness and photometric errors are included using the artificial star experiments described in Section 2 and a mock catalogue of masses and distances is created. The corrections to the guess MF are calculated by comparing the distribution of

[3] https://people.smp.uq.edu.au/HolgerBaumgardt/globular/

synthetic and observed stars in the mass-distance plane, and the updated MF is used as input for the next iteration. This algorithm converges after a few iterations providing the output global MF.

Specifically, the algorithm can be schematically summarized as follows:

(i) An initial guess of the MF (defined by the coefficients k_i) is made. In the present analysis the coefficients corresponding to a Kroupa (2001) IMF have been adopted as first guess.

(ii) A synthetic stellar population has been created by extracting 10^6 stars from the adopted MF with masses between 0.1 and 8 $M_\odot$. It has been assumed that the mass loss of stars with masses $<M_{\rm tip}$ (the mass at the tip of the red giant branch, RGB) is negligible while those with masses $>M_{\rm tip}$ have been evolved into white dwarfs (WDs) following the initial–final mass relation of Kaliari et al. (2009):

$$m_{\rm WD} = 0.109\, m + 0.428. \tag{13}$$

According to the upper limit of the IMF, the WDs are all retained by the GC unlike the other types of compact remnants. This implicitly assumes that the neutron stars and the black holes are ejected during the GC evolution by natal kicks and/or the Spitzer instability (Spitzer 1987). The fraction of mass in remnants in each bin (ν_i) has also been calculated. No binaries have been simulated. These objects constitute only a small (< 5 per cent) fraction of objects in GCs (Milone et al. 2012) and their presence is not expected to significantly affect the final MF.

(iii) The corresponding V and I magnitudes of the synthetic stars have been derived by interpolating the masses of visible stars through the mass–luminosity relation of the adopted isochrone from the Dotter et al. (2007) database, adopting the best-fitting metallicity, age, distance modulus, and reddening provided by Dotter et al. (2010; see Section 2). Zero luminosity in both bands has been assumed for the population of remnants. Note that we used the same isochrone, distance modulus, and reddening for each GC, both in photometric data reduction and in MF analysis processes.

(iv) A synthetic population of field stars has been derived from the Galactic model provided by Robin et al. (2003) covering an area of 1 deg^2 around each GC centre and the V and I magnitudes have been transformed into the *HST*/ACS photometric system using the transformation provided by Sirianni et al. (2005).

(v) We defined eight evenly spaced mass groups ranging from 0.1 $M_\odot$ to $M_{\rm tip}$ and one additional bin for stars more massive than $M_{\rm tip}$ including massive WDs. Eight *I*-band magnitude intervals containing the above defined mass bins (excluding the one related to remnants) have been also defined accordingly. Real field and synthetic stars with colours within three times the mean locus of MS stars have been binned in these groups. The projected density of field stars in each bin $\Gamma_i^{\rm field}$ is calculated by dividing the number of field stars contained in each mass bin by the area of the extracted field catalogue (1 deg^2).

(vi) The completeness factor, $C(m, R)$, defined as the fraction of artificial stars recovered in each magnitude (mass) bin and contained in concentric annular regions of 0.1 arcmin width, has been estimated.

(vii) The azimuthal coverage of the observational field of view as a function of the projected distance, Az(R), has been calculated.

(viii) We compute the value of the log-likelihood function defined as

$$\log\, L = \sum_{j=1}^{N_{\rm tot}^{\rm obs}} \log[P(m_j, R_j)], \tag{14}$$

where $N_{\rm tot}^{\rm obs}$ is the total number of observed stars, m_j and R_j are the mass and projected distance of the jth observed star, and $P(m_j, R_j)$ is the total probability density function to find a star with mass m_j at a projected distance from the centre R_j. This last function is calculated as the model density in the m–R plane, after correcting for completeness and azimuthal coverage,

$$P(m_j, R_j) = \left[\frac{N_{\rm tot}^{\rm obs} - N_{\rm tot}^{\rm field}}{\sum_{i=1}^{H} N_i}\Gamma(m_j, R_j)(1-\nu_j) + \Gamma_j^{\rm field}\right] \times \frac{C(m_j, R_j)\, Az(R_j)}{N_{\rm tot}^{\rm obs}}, \tag{15}$$

where N_i and $\Gamma(m_j, R_j)$ are calculated from equations (4) and (5), $\Gamma_i^{\rm field}$ is the projected number density of field star in the same mass bin of the jth star, $N_{\rm tot}^{\rm obs}$ is the total number of stars in the observed catalogue, and

$$N_{\rm tot}^{\rm field} = \sum_{i=1}^{H} \Gamma_i^{\rm field} \int_0^{r_t} 2\pi R\, C(m_i, R)\, {\rm Az}(R) {\rm d}R.$$

(ix) For the guess choice of k_i, the W_0, r_c space has been searched to find the values maximizing the above merit function using Powell's direction set algorithm (Brent 1973).

(x) For the best-fitting pair of (W_0, r_c) values, the corresponding multimass model has been computed. Synthetic stars have been distributed according to the density profile of their corresponding mass bin across the field of view.

(xi) For each synthetic star, a particle from the artificial star library with I magnitude within 0.25 mag and the distance from the GC centre within 0.1 arcmin, with respect to the same quantities of the given star, has been selected and, if recovered (see Section 2), its output–input magnitude and colour shift have been added to those of the corresponding star. The same procedure has been applied to field stars.

(xii) For each synthetic star located at a distance R_j from the centre, a random number η uniformly distributed between 0 and 1 has been extracted and the star is rejected if $\eta >$ Az(R_j). The same procedure has been applied to field stars. At the end of this step a mock catalogue of synthetic stars corresponding to the guess choice of k_i, W_0, and r_c is obtained, accounting for the photometric errors, incompleteness, and azimuthal coverage.

(xiii) The number of stars in the observed ($N_i^{\rm obs}$), field ($N_i^{\rm field}$), and synthetic ($N_i^{\rm mock}$) catalogues contained in the eight I magnitude bins have been counted and the k_i coefficients have been updated using the relation

$$k_i' = k_i \frac{N_{\rm tot}^{\rm mock}\left(N_i^{\rm obs} - N_i^{\rm field}\right)}{\left(N_{\rm tot}^{\rm obs} - N_{\rm tot}^{\rm field}\right) N_i^{\rm mock}} \tag{16}$$

The entire procedure has been repeated iteratively until convergence. The global MF is determined by the relative number of stars in the eight mass bins in the last iteration (equation 4).

The best fit of the projected density profiles for two GCs and of the distribution of stars in the m–R plane for NGC 5286 are shown in Figs 3 and 4, as an example. According to Fig. 4, the density contours of the best-fitting model are generally in good agreement with the distribution of stars in the m–R plane. As an alternative view, in Fig. 3, the surface density predicted by the best-fitting model for three mass groups is overplotted to the observational density profile for the same GCs. Note that, while the model captures the general

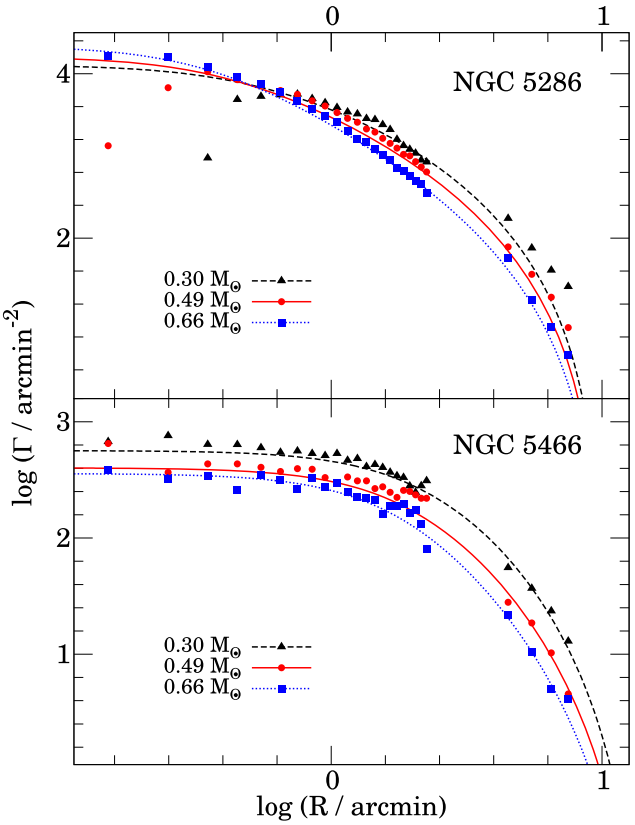

Figure 3. Projected density profiles for three mass groups in two GCs: NGC 5286 (top panel) and NGC 5466 (bottom panel). Coloured dots mark completeness-corrected densities of different mass groups. The density profile of the best-fitting models are shown with solid, dotted, and dashed lines. The same plot for the entire sample of GCs is available as Supporting Information in the online version of the paper.

behaviour of mass segregation, some discrepancies are apparent inside the core of these GCs.

The stellar mass of each GC has been derived by normalizing the total number of stars in the best-fitting model to those counted in the observed catalogue:

$$M_{\rm lum} = \frac{N_{\rm tot}^{\rm obs} - N_{\rm tot}^{\rm field}}{N_{\rm tot}^{\rm mock}} \sum_{i=1}^{H} N_i m_i (1 - \nu_i). \quad (17)$$

The dynamical mass has been estimated by comparing the observed velocity dispersion profile with the prediction of the best-fitting model. In particular, the mass of the model has been chosen as the one minimizing the penalty function:

$$\mathcal{L} = \sum_{j=1}^{N} \left\{ \frac{(v_j - \bar{v})^2}{\sigma^2_{{\rm LOS},8}(R_j) + \epsilon_j^2} + \ln\left[\sigma^2_{{\rm LOS},8}(R_j) + \epsilon_j^2\right] \right\}, \quad (18)$$

where N is the number of radial velocities, v_j is the radial velocity of the jth star, $\bar{v}$ is the mean velocity of the sample, ϵ_j is the uncertainty of the radial velocity and $\sigma_{{\rm LOS},8}(R_j)$ is the line-of-sight velocity dispersion predicted by the best-fitting model at the projected distance R_j of the jth star for the eighth mass group (see equation 6). The choice of the eighth bin is justified by the fact that the considered radial velocity catalogues contain stars along the RGB covering a limited range of masses.

The total V-band luminosity has been calculated using equation (11), allowing to derive the mass-to-light ratio, $M_{\rm dyn}/L_V$.

The fraction of dark remnants has been estimated using the following relation:

$$f_{\rm remn} = 1 - \frac{M_{\rm lum}}{M_{\rm dyn}}. \quad (19)$$

The half-mass radius, $r_{\rm h}$, has been evaluated as the radius including half of the GC mass while the half-mass relaxation time as (Spitzer 1987)

$$t_{\rm rh} = 0.138 \frac{M_{\rm dyn}^{1/2} r_{\rm h}^{3/2}}{G^{1/2} \bar{m} \ln(\gamma M_{\rm dyn}/\bar{m})}, \quad (20)$$

where $\gamma = 0.11$ (Giersz & Heggie 1996) and $\bar{m}$ is the mean mass of stars (equation 7).

5 RESULTS

5.1 An overview of GCs' mass function and their parameters

The derived global MFs and the structural/dynamical parameters of 32 GCs are listed in Table 2 and the present-day MFs of these GCs are shown in Fig. 5. The MF slopes α calculated by fitting a single power law, $F(m) \propto m^{\alpha}$, in the mass range $0.2 < m/{\rm M}_{\odot} < 0.8$ have also been calculated.

In the considered sample, the derived parameters cover wide ranges in MF slope ($-1.26 < \alpha < 0.02$), mass ($2.2 \times 10^4 < M/{\rm M}_{\odot} < 10^6$), mass-to-light ratio ($0.4 < M/L_V < 2.9$), and half-mass radius ($4 < r_{\rm h}/{\rm pc} < 17.6$). For reference, a Kroupa (2001) IMF in this mass range has an average slope of -1.567. As already found in SB17, GCs with a steeper MF slope tend to have a convex shape with a systematic depletion of stars at $M < 0.2$ M$_{\odot}$, while the MF of GCs with a flatter MF are much better fitted by single power laws.

5.2 Dependence on assumptions: NGC 104 as test case

The MF of the GC NGC 104 has been studied by de Marchi & Paresce (1995) who used *HST*/WFPC2 observations at 4.6 arcmin from the centre through F606W and F814W filters, i.e. similar to one of the ACS pointing used in the present analysis (P2 in Fig. 1; at $\sim 6'$), adopting a different distance and mass-luminosity relation. The MF slope calculated from this work in the range $-0.60 < \log(m/{\rm M}_{\odot}) < -0.15$ turns out to be $\alpha = -1.15$, flatter than what is estimated in the present work ($\alpha = -1.26$). This gives the opportunity to test the effect of the various assumptions on the derived MF providing also a validation of the photometric analysis and completeness correction with a completely independent study. Note that our analysed region is located on the opposite side of the de Marchi & Paresce (1995) field with respect to the cluster centre and is larger. In the top panel of Fig. 6 the luminosity functions of de Marchi & Paresce (1995) and our 'P2' region are compared, with and without applying the completeness correction. A good agreement between the two works is apparent, with only random fluctuations of <0.1 dex amplitude and no systematic trend. This is particularly apparent when completeness correction are applied in both works, accounting for the different depth of the two different observations. This agreement indicates that the difference in the MF slope between these two works does not depend on either the photometry or on the completeness, but on the different assumptions on distance and/or mass–luminosity relation.

de Marchi & Paresce (1995) derived the MF of stars within their region using a Bergbusch & VandenBerg (1992) isochrone with [Fe/H] $= -0.65$ and age of 14 Gyr for NGC 104 and adopt a distance of 4.6 kpc (Webbink 1985), while in this work we use

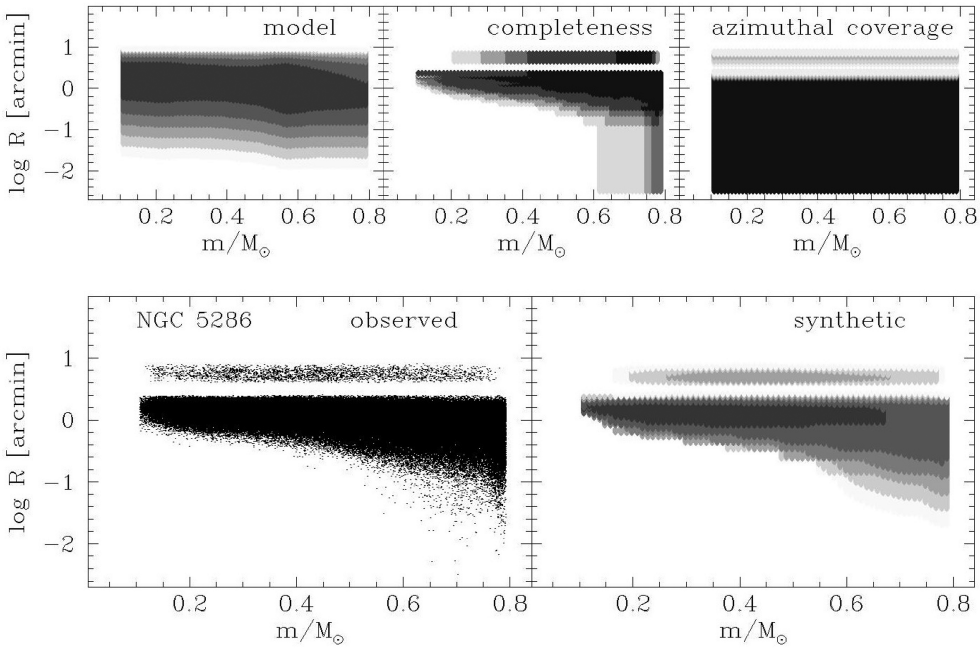

Figure 4. Distribution of stars in the m–$\log R$ plane for NGC 5286 (bottom-left panel). The probability densities predicted by the corresponding best-fitting final models (bottom-right panel), initial model prediction (top-left panel), the completeness (top-middle panel), and the azimuthal coverage (top-right panel) are shown.

Table 2. Parameters of the best-fitting models.

NGC	α	$\log(M_{\rm lum}/{\rm M}_\odot)$	$\log(M_{\rm dyn}/{\rm M}_\odot)$	$r_{\rm h}$ (pc)	$f_{\rm remn}$	$t_{\rm rh}$ (Gyr)	$M_{\rm dyn}/L_V$ ($M_\odot/L_\odot$)	$r_{\rm J}$ (pc)
104	− 0.45 ± 0.12	5.574 ± 0.008	5.958 ± 0.012	6.024 ± 0.032	0.586 ± 0.014	4.946	2.022 ± 0.068	183.96
288	− 0.75 ± 0.05	4.638 ± 0.056	5.024 ± 0.033	10.121 ± 0.292	0.589 ± 0.061	5.075	2.084 ± 0.311	137.32
362	− 0.79 ± 0.05	5.110 ± 0.011	5.517 ± 0.029	4.811 ± 0.071	0.608 ± 0.028	2.455	1.339 ± 0.096	208.88
1261	− 0.72 ± 0.04	4.912 ± 0.011	5.260 ± 0.044	6.882 ± 0.064	0.551 ± 0.047	3.167	1.489 ± 0.156	190.57
1851	− 0.74 ± 0.04	5.113 ± 0.009	5.606 ± 0.026	5.631 ± 0.015	0.678 ± 0.020	3.375	1.861 ± 0.118	234.49
2298	− 0.05 ± 0.06	4.279 ± 0.011	4.596 ± 0.161	5.856 ± 0.324	0.518 ± 0.179	1.292	0.852 ± 0.317	98.74
3201	− 1.22 ± 0.10	4.936 ± 0.011	5.266 ± 0.024	8.779 ± 0.339	0.532 ± 0.028	5.395	1.748 ± 0.106	71.63
4590	− 1.25 ± 0.08	4.821 ± 0.012	5.099 ± 0.044	8.740 ± 0.077	0.472 ± 0.055	4.754	1.837 ± 0.193	78.89
5024	− 1.21 ± 0.08	5.399 ± 0.010	5.588 ± 0.041	11.136 ± 0.013	0.370 ± 0.061	10.567	1.361 ± 0.132	213.65
5053	− 1.26 ± 0.04	4.482 ± 0.012	4.733 ± 0.115	17.621 ± 0.110	0.439 ± 0.149	10.337	1.648 ± 0.439	107.33
5272	− 1.02 ± 0.08	5.369 ± 0.009	5.669 ± 0.024	8.270 ± 0.016	0.498 ± 0.030	6.981	1.595 ± 0.094	186.08
5286	− 0.64 ± 0.04	5.281 ± 0.010	5.579 ± 0.021	5.016 ± 0.019	0.496 ± 0.027	2.789	1.129 ± 0.060	143.73
5466	− 1.14 ± 0.06	4.603 ± 0.012	4.763 ± 0.090	16.192 ± 0.130	0.308 ± 0.145	8.617	1.162 ± 0.243	96.28
5897	− 1.06 ± 0.14	4.844 ± 0.011	5.329 ± 0.045	11.527 ± 0.157	0.672 ± 0.035	8.142	2.906 ± 0.311	105.57
5904	− 0.81 ± 0.08	5.216 ± 0.010	5.615 ± 0.022	6.773 ± 0.101	0.601 ± 0.022	4.603	1.863 ± 0.104	106.70
5986	− 0.58 ± 0.05	5.135 ± 0.010	5.581 ± 0.042	5.377 ± 0.063	0.642 ± 0.036	3.029	1.719 ± 0.171	103.72
6093	− 0.16 ± 0.05	5.053 ± 0.010	5.578 ± 0.030	4.056 ± 0.067	0.701 ± 0.022	1.872	1.540 ± 0.112	89.84
6101	− 1.24 ± 0.12	4.906 ± 0.095	5.222 ± 0.075	13.732 ± 0.086	0.516 ± 0.135	10.199	1.773 ± 0.493	84.86
6144	0.02 ± 0.07	4.329 ± 0.010	4.344 ± 0.491	5.569 ± 0.384	0.034 ± 1.092	0.939	0.416 ± 0.470	21.78
6218	− 0.36 ± 0.06	4.654 ± 0.009	5.026 ± 0.031	5.232 ± 0.147	0.576 ± 0.032	1.640	1.587 ± 0.118	60.57
6254	− 0.57 ± 0.10	4.937 ± 0.009	5.335 ± 0.032	5.815 ± 0.093	0.599 ± 0.031	2.685	1.716 ± 0.132	74.75
6341	− 0.77 ± 0.05	5.128 ± 0.010	5.513 ± 0.032	5.599 ± 0.019	0.588 ± 0.032	3.269	1.571 ± 0.121	149.10
6362	− 0.58 ± 0.07	4.729 ± 0.013	5.192 ± 0.035	8.456 ± 0.244	0.655 ± 0.030	4.173	1.991 ± 0.171	93.25
6541	− 0.55 ± 0.05	5.064 ± 0.011	5.506 ± 0.052	5.096 ± 0.071	0.639 ± 0.044	2.654	1.718 ± 0.210	47.17
6584	− 0.78 ± 0.06	4.745 ± 0.010		7.760 ± 0.082				
6723	− 0.16 ± 0.06	4.772 ± 0.009	5.227 ± 0.034	4.989 ± 0.083	0.650 ± 0.028	1.726	1.789 ± 0.144	49.12
6752	− 0.43 ± 0.08	4.996 ± 0.010	5.289 ± 0.005	5.652 ± 0.118	0.490 ± 0.013	2.409	1.303 ± 0.032	102.06
6779	− 0.59 ± 0.05	4.823 ± 0.010	5.384 ± 0.081	6.291 ± 0.104	0.725 ± 0.052	3.305	1.955 ± 0.368	119.02
6809	− 0.83 ± 0.07	4.935 ± 0.011	5.283 ± 0.028	7.289 ± 0.106	0.551 ± 0.031	3.922	1.767 ± 0.122	79.93
7078	− 1.00 ± 0.04	5.448 ± 0.010	5.820 ± 0.018	6.508 ± 0.015	0.575 ± 0.020	5.856	1.608 ± 0.077	223.09
7089	− 0.72 ± 0.06	5.415 ± 0.008	5.954 ± 0.029	6.127 ± 0.015	0.711 ± 0.020	5.495	2.238 ± 0.155	287.75
7099	− 0.80 ± 0.03	4.771 ± 0.013	5.136 ± 0.026	5.369 ± 0.088	0.569 ± 0.029	2.198	1.620 ± 0.109	136.80

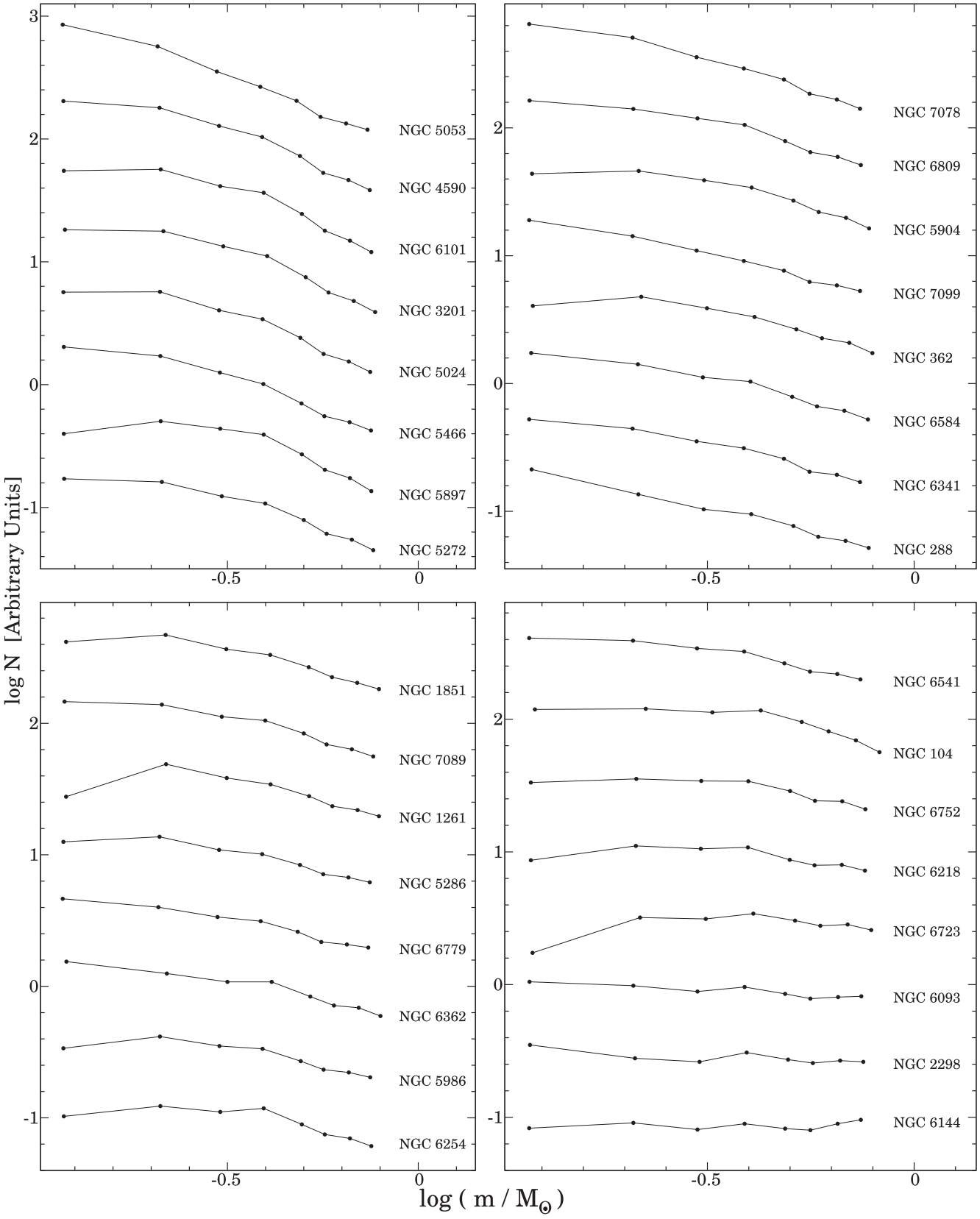

Figure 5. Present-day mass function of the 32 GCs in our sample. A vertical shift has been added to each cluster in each panel for clarity. From left to right panels and top to bottom panels, GCs have been sorted according to their MF slope, in descending order.

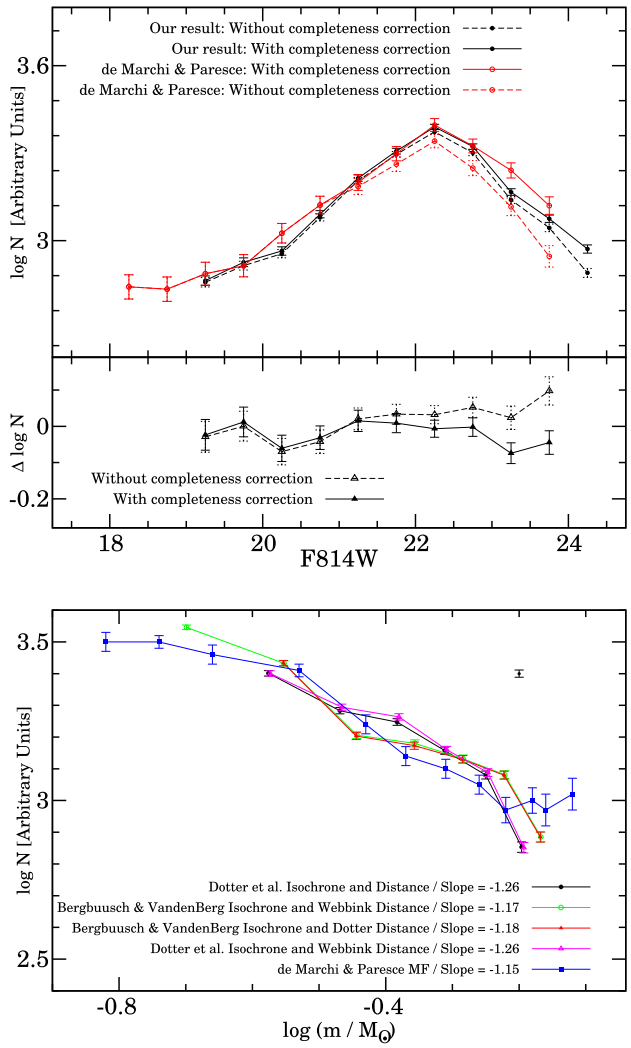

Figure 6. Comparisons between the luminosity function (top panel) and MF (bottom panel) of our analysed P2 region against de Marchi & Paresce (1995) region in NGC 104. The difference of the luminosity function between the two works calculated for raw and completeness corrected luminosity functions is shown in the lower box of the top panel. The MF slope reported in the bottom panel has been calculated in the mass range $-0.60 < \log(m/M_{\odot}) < -0.15$. The error bars are related to Poisson errors estimated from counting statistics. An arbitrary shift has been added to each MF and luminosity function for clarity.

a Dotter et al. (2007) isochrone with [Fe/H] $= -0.7$ and age of 12.75 Gyr and adopt a distance of 4.5 kpc.

To check the effect of such assumptions we derived the MF of region P2 using all the combinations of isochrones (Bergbusch & VandenBerg 1992; Dotter et al. 2007) and distance moduli (Webbink 1985; Dotter et al. 2007), and compared these four resulting MFs with the MF derived by de Marchi & Paresce (1995) in their analysed field. In the bottom panel of Fig. 6 this comparison is shown. It is clear that the small difference in the adopted distance produces a negligible effect across the entire mass range. A larger effect is produced by the different mass–luminosity relation, with the Bergbusch & VandenBerg (1992) isochrone providing a flatter MF than that derived using Dotter et al. (2007) models ($\Delta\alpha \sim 0.1$). So, this effect can entirely explain the difference in the measured slope.

Summarizing, at least for the case of NGC 104, the impact of assumptions on distance and adopted models should not produce an effect exceeding $\Delta\alpha \sim 0.15$ in the MF slope.

5.3 Comparison with previous works

In this section we compare the results obtained in this analysis with those obtained by SB17 and Paust et al. (2010) (who applied a similar technique using only data in the central cluster region) and with those by BH18. The statistics of the differences between our work with those mentioned above have been summarized in Table 3.

In Fig. 7, the MF slopes and half-mass radii of 28 GCs and the dynamical masses and the mass-to-light ratios of 23 GCs in common between this work and SB17 are compared. The largest differences in the estimated MF slopes ($\Delta\alpha > 0.2$) are related to the two GCs which have the steepest MF among 28 GCs in SB17 (e.g. NGC 5466 and NGC 6101) while they have flatter MF in this work. The mean differences between the two studies indicate good agreements in estimated MF slopes, dynamical masses, and mass-to-light ratios. The difference between two studies in estimated half-mass radii shows that the three GCs with the largest difference between the half-mass radii estimated in these works, i.e. NGC 6101, NGC 5466, NGC 5024, are those with the largest difference in the estimated MF slope. This indicates the importance of the MF constraint outside the ACS field of view for these extended clusters.

15 GCs are in common with the work by Paust et al. (2010). While the difference between these two works is not statistically significant, our MFs are on average flatter than those measured by Paust et al. (2010). These authors used the same *HST*/ACS photometric data in the central region and the same multimass model fitted in an annular region close to the half-light radius.

In Fig. 8, the half-mass radii of 32 GCs, masses, and mass-to-light ratios of the 31 GCs in common between this work and BH18 are compared. These authors determined the masses and structural/dynamical parameters of GCs by fitting a large set of *N*-body simulations to the velocity dispersion profile from the same set of radial velocities adopted in this work. The mean differences in the estimated masses and *M*/*L* ratios indicate good agreement within the errors in spite of the difference between our adopted multimass models and *N*-body simulation. The estimated half-mass radii are instead slightly larger in this work. This difference arises mainly from the more compact GCs, where the constraint provided by the external field photometry tends to favour a slightly larger mass at large radii.

5.4 Mass segregation

The MFs derived here rely on the assumption that King-Michie multimass models (computed according to the prescriptions of Gunn & Griffin 1979) provide an adequate description of the mass segregation occurring in GCs. It is interesting to check this hypothesis by comparing the predicted and observed variation of the MF slope at different distances from the cluster centre.

For this purpose, we considered for each GC five regions at different distances from the cluster centre: four annular regions of 0.4 arcmin width in the central field and a single bin containing the parallel pointings. Then We computed the completeness-corrected MF slopes at these radial bins. The radial behaviour of MF slopes measured in two GCs (NGC 5286 and NGC 5466) is compared with those predicted by the best-fitting model in Fig. 9. It is clear that the model reproduces well the observed radial trend of the MF slope for NGC 5466, while it does not match the MF slope

Table 3. The mean (μ) and standard deviation (σ) of differences between this work and the others in estimated MF slopes (third column), dynamical masses (fourth column), half-mass radii (fifth column), and mass-to-light ratios (sixth column).

	Statistic	$\Delta\alpha$	$\Delta\log(M/\mathrm{M}_\odot)$	$\Delta\log(r_\mathrm{h}/\mathrm{pc})$	$\Delta[(M/\mathrm{M}_\odot)/(L/\mathrm{L}_\odot)]$
This work – Paust et al. (2010)	μ	0.23 ± 0.12			
	σ	0.43			
This work – BH18	μ		0.04 ± 0.02	0.10 ± 0.01	-0.27 ± 0.08
	σ		0.11	0.08	0.46
This work – SB17	μ	0.03 ± 0.03	0.005 ± 0.020	0.02 ± 0.02	-0.10 ± 0.06
	σ	0.16	0.10	0.10	0.31

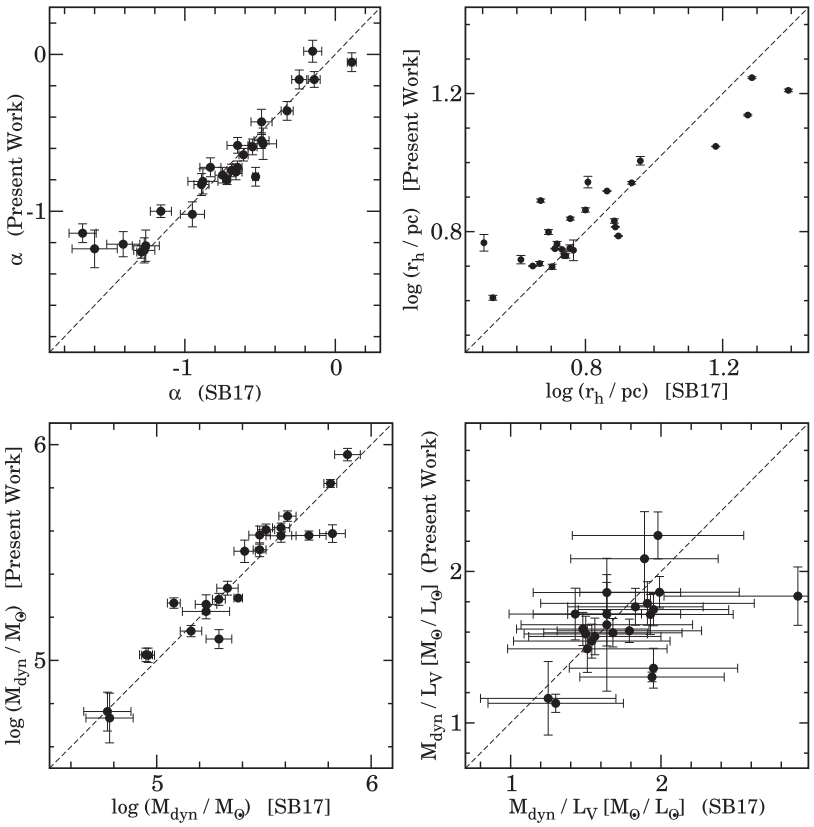

Figure 7. Comparison between the MF slopes (top-left panel), half-mass radii (top-right panel), dynamical masses (bottom-left panel), and mass-to-light ratios (bottom-right panel) derived in this work and those determined by SB17. The one-to-one relation is marked by the dashed line.

variation in NGC 5286. In particular, in this last GC the observed MF slope varies much more quickly (by $\Delta\alpha \sim -6$) with radius than what is predicted by the best-fitting model ($\Delta\alpha \sim -1.2$). In other words, NGC 5286 appears to be oversegregated with respect to the prediction of the King-Michie model.

To quantify the discrepancy between models and observations, for each GC we performed a least-squares fit to the residuals of the best-fitting MF slope ($\Delta\alpha$) as a function of the distance from the centre (in units of r_h) and adopted the slope of this linear fit $\xi \equiv \mathrm{d}\Delta\alpha/\mathrm{d}\log R$ as an indicator of the observed oversegregation. The oversegregation parameter measured in the whole GCs sample is plotted as a function of the projected central density and half-mass density in Fig. 10. Both densities clearly correlate with ξ such that, while at relatively small densities models correctly reproduce the observed degree of mass segregation ($\xi \sim 0$), denser GCs show significantly steeper gradients of α ($\xi < 0$). Note that ξ does not seem to significantly correlate with other quantities. This evidence can be interpreted in two alternative ways: (i) the estimated completeness is spuriously high in the extremely crowded conditions occurring in dense GCs or (ii) this is a real effect such that the densest GCs with shorter central relaxation time reach a degree of mass segregation higher than what is predicted by multimass models. In this context, it is interesting to note that the correlation with the central projected density (an indicator of the maximum crowding) has a larger spread than that with the half-mass density (which is an intrinsic parameter of the GC).

Note that the global MF slopes (listed in Table 2) are strongly constrained by the radial interval close to the half-mass radius containing the largest fraction of stars. So, while any inadequacy of the adopted models reflects in the accuracy of the estimated MF slopes, no significant systematic errors are expected. This fact is supported by the simulations of Baumgardt & Makino (2003) who

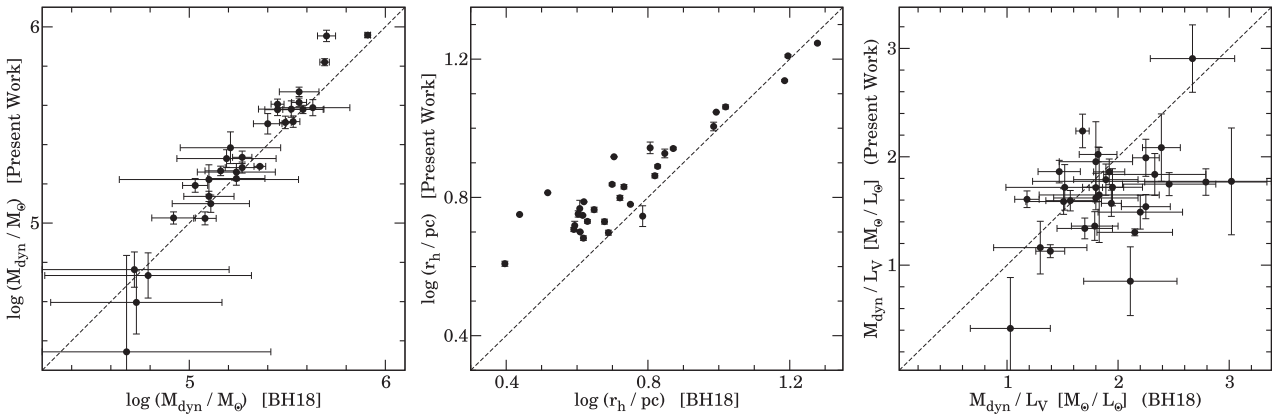

Figure 8. Comparison between the dynamical masses (left-hand panel), half-mass radii (middle panel), and mass-to-light ratios (right-hand panel) derived in this work and those determined by BH18. The one-to-one relation is marked by the dashed line.

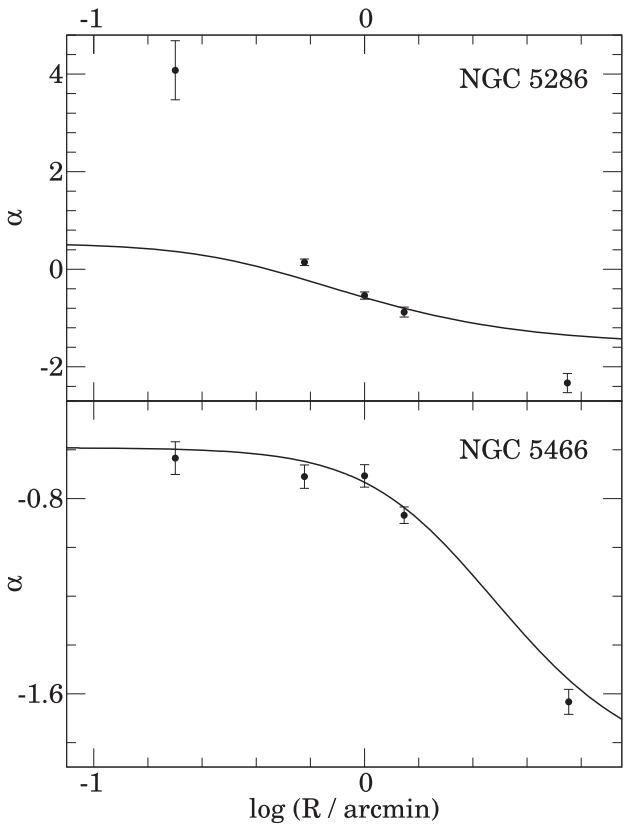

Figure 9. Radial variation of the MF slopes of two GCs: NGC 5286 (top panel) and NGC 5466 (bottom panel). The slope predicted by the corresponding best-fitting model is shown by solid lines.

found that the global and local MFs at around 60 per cent of the half-light radius are approximately the same.

5.5 Tidal radii of GCs

We calculated the present-day Jacobi radius (r_J; defined as the distance of the inner Lagrangian point from the cluster centre) of each GC in our sample using the same formulas described in Sollima & Mastrobuono Battisti (2014; see their appendix A2). For this purpose, we used the dynamical masses estimated here and the velocities from *Gaia* DR2 determined by Baumgardt et al. (2019). We have assumed a three-component Galactic potential given by the superposition of (i) a Hernquist bulge with $c = 0.7$ kpc and $M_b = 1.3 \times 10^{10}\,M_\odot$, (ii) a Miyamoto & Nagai disk with $a = 6.5$ kpc, $b = 0.26$ kpc and $M_d = 1.085 \times 10^{11}\,M_\odot$, (iii) a logarithmic halo with $v_0 = 165\,km\,s^{-1}$ and $d = 12$ kpc {in analogy with the potential adopted by Johnston, Spergel & Hernquist (1995), with a slightly different normalization of the components to best fit the post-*Gaia* Galactic kinematics of GCs; Sollima et al., in preparation].

In Fig. 11, the ratio of the half-mass radius to the Jacobi radius as a function of Galactocentric distance derived from Harris (1996, 2010 edition) is shown. Among the innermost GCs with $R_{GC} < 8$ kpc, two extreme cases are notable: (i) NGC 6144 has the highest ratio ($r_h/r_J = 0.26$) because it is the lightest and one of the nearest GCs from the centre of the Galaxy, (ii) The lowest ratio belongs to NGC 104 with $r_h/r_J = 0.03$ which is the most massive GC in our sample and the most distant GC from the centre of the Galaxy within the mentioned interval. Generally, there is no clear relationship between r_h/r_J and R_{GC} in this interval. For outer GCs with $R_{GC} > 8$ kpc, there are two recognizable groups: (i) 5 GCs with $r_h/r_J > 0.08$, i.e. NGC 3201, NGC 4590, NGC 5053, NGC 5466, and NGC 6101 whose mean mass and mean half-mass radii are $M_{dyn} \approx 10^5\,M_\odot$ and $r_h \approx 13$ pc respectively, so they are the extended and tidally filling GCs. (ii) 12 GCs with $r_h/r_J \lesssim 0.08$. Their mean mass and mean half-mass radii are $M_{dyn} \approx 3.2 \times 10^5\,M_\odot$ and $r_h \approx 7$ pc, respectively. Most of the GCs in this group are compact and tidally underfilling.

The GCs in the former group experience a stronger tidal field and are expected to dissolve faster than the ones in the latter group. The existence of these two distinct groups confirms the previous findings by Baumgardt et al. (2010).

5.6 Analysis of correlations

Our sample of GCs constitutes a large enough data set to investigate the correlations between MF slope and the dynamical, structural and orbital parameters. The following parameters have been considered: the Galactocentric distance (R_{GC}), distance from Galactic plane (Z), the average apogalactic (R_{apo}) and perigalactic (R_{per}) distance and the average dissolution time (t_{diss}) derived by Baumgardt et al. (2019), the concentration (c) derived from McLaughlin & van der Marel (2005), the age (t_{age}) and metallicity ([Fe/H]) derived by Dotter et al. (2010), the luminous mass (M_{lum}), dynamical mass (M_{dyn}), remnant mass fraction (f_{remn}), V-band magnitude (M_V),

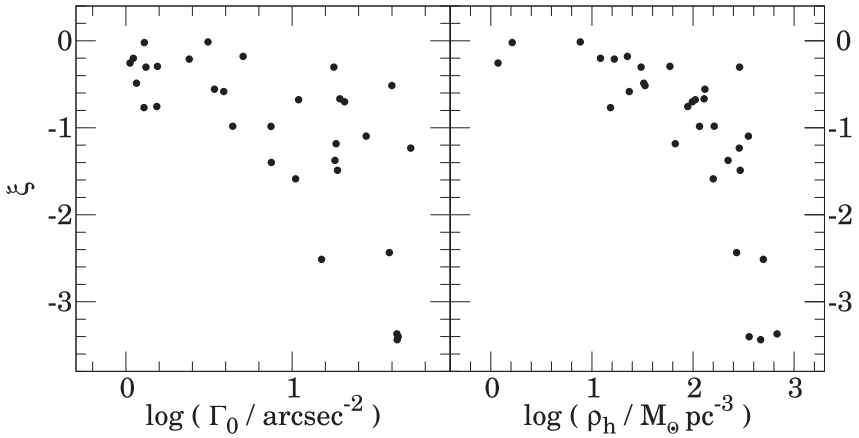

Figure 10. Projected central density (left-hand panel) and half-mass density (right-hand panel) versus ξ for all GCs in our sample.

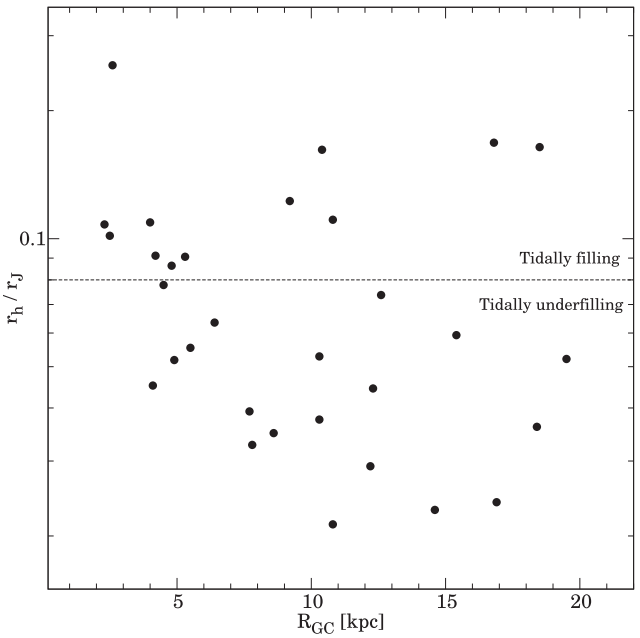

Figure 11. Ratio of half-mass radius to Jacobi radius ($r_{\rm h}/r_{\rm J}$) versus Galactocentric distance for 31 Galactic GCs. The dashed line empirically separates tidally underfilling from tidally filling GCs.

mass-to light ratio ($M_{\rm dyn}/L_V$), half-mass radius ($r_{\rm h}$), half-mass relaxation time ($t_{\rm rh}$) and half-mass density ($\rho_h \equiv 3M_{\rm dyn}/(8\pi r_h^3)$), all derived from our adopted best-fitting model.

We have employed a permutation test to calculate the significance of the univariate correlations between MF slope and the other parameters. For each parameter, an error-weighted least-squares fit has been performed and the corresponding χ^2 value has been estimated. The same process has been performed on 10^4 realizations simulated by randomly swapping the values of the independent variable. The significance of the correlation is defined by the fraction of realizations with a χ^2 larger than the one calculated in the observed sample. The complete set of correlations and their related probabilities are shown in Fig. 12. We found a tight anticorrelation with $P > 99.7$ per cent between the present-day MF slope and the following parameters: $t_{\rm rh}$, $r_{\rm h}$, $R_{\rm GC}$, $\log|Z|$, $\log R_{\rm apo}$, $\log R_{\rm per}$ and $\log t_{\rm diss}$, and marginal (95 per cent $< P <$ 99.7 per cent) correlations with $\log \rho_{\rm h}$ and $f_{\rm remn}$. Note that most of these parameters are correlated to each other so that it is not easy to distinguish the leading parameter determining the correlation.

The anticorrelation with half-mass relaxation time confirms what was found in SB17. The left-hand panel of Fig. 13 shows another view of the correlation between MF slope and the ratio between the GC age and present-day half-mass relaxation time. The tight correlation is clear: less-evolved GCs have the steeper MFs. It is apparent in this plot that an increase of α by a factor of 2 between $\alpha \approx -1.2$ and $\alpha \approx -0.6$ implies an increase of $t_{\rm age}/t_{\rm rh}$ by a factor of 5. Only a marginal correlation is instead found with the remnant fraction, as claimed in Sollima & Baumgardt (2017).

Moreover, the correlations with the present-day Galactic position (found by Djorgovski et al. 1993; Capaccioli et al. 1993; Piotto & Zoccali 1999) are also confirmed.

Instead, the correlation with concentration, previously reported by de Marchi et al. (2007), is found to be not significant.

As explained above, there are a lot of significant correlations between individual parameters and the MF slope. Some of these parameters are expressible in terms of each other so that the significance of their univariate correlation with the MF slope cannot be interpreted as a proof of the physical dependence of the MF on these parameters. For instance, both the Galactocentric distance and half-mass relaxation time separately show significant correlations with the MF slope. However, GCs at large Galactocentric distances have on average large half-mass radii (van den Bergh, Morbey & Pazder 1991) and thus long relaxation times. So, the correlation with Galactocentric distance can be driven by the effect of the relaxation time rather than by the current location in the Galaxy.

To avoid this problem, we also considered the bivariate correlations of all the possible pairs of parameters listed above. In this case, for any pair of variables a bilinear fit is performed providing a χ^2_{biv}. A permutation test by randomly swapping the second independent variable is then performed providing 10^4 individual χ^2_{perm}. The second independent variable is considered an independent correlator if the fraction of random realizations with a $\chi^2_{perm} > \chi^2_{biv}$ is larger than 99.7 per cent. This test allows us to identify the strongest among two correlating variables. Indeed, if we adopt $t_{\rm age}/t_{\rm rh}$ as the first independent variable, the only significant bivariate correlator would be metallicity. Instead, if we assumed any other parameter as the first independent variable, we would find the only significant bivariate correlation using $t_{\rm rh}$ as the second independent variable. This indicates that the driving parameter in determining the MF slope is the half-mass relaxation time, while all the other correlations

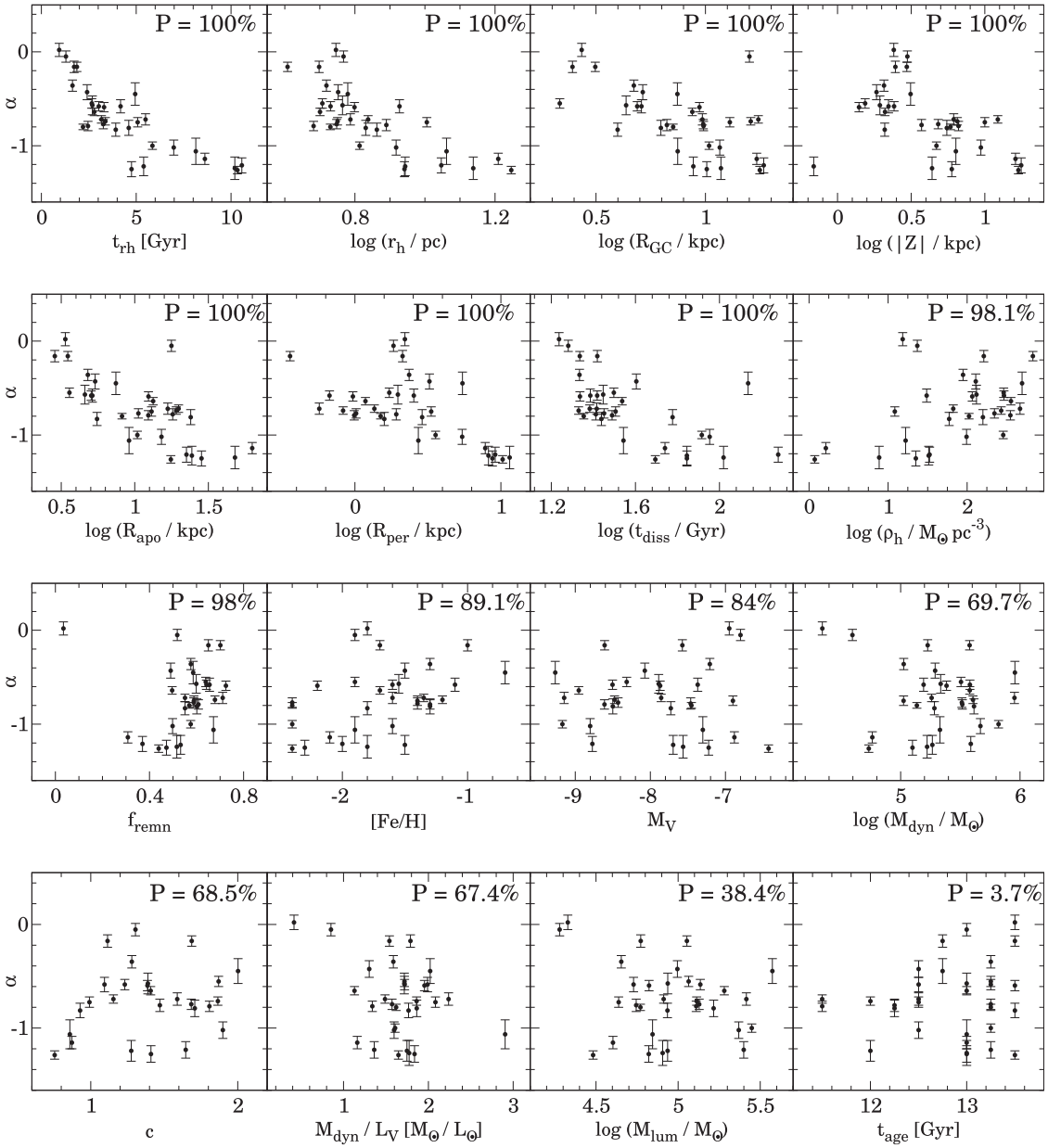

Figure 12. Univariate correlations between the global MF slope α and various dynamical, structural, and orbital parameters. The statistical significance (P) of each correlation is indicated.

are only consequences of implicit covariances. In other word, the residuals of a fit in the $\alpha - t_{\rm rh}$ plane correlate with metallicity only.

In the right-hand panel of Fig. 13, the residual of the least-squares fit in the $\alpha - \log(t_{\rm age}/t_{\rm rh})$ plane

$$\alpha = (1.17 \pm 0.12)\log(t_{\rm age}/t_{rh}) - (1.35 \pm 0.07)$$

are shown as a function of metallicity. The slope of the apparent trend is $d\alpha/d[Fe/H] \sim 0.37$. We note that most of this correlation is driven by two GCs at the metal-poor end (NGC 4590 and NGC 7099) and by the most metal-rich GC of our sample (NGC 104).

6 DISCUSSION

In this paper, we performed the deepest photometry of *HST*/ACS/WFC parallel fields for 32 Galactic GCs, combined them with *HST* data available for the central regions of these GCs from the *ACS Treasury Program* (Sarajedini et al. 2007), and compared this data set with multimass dynamical models to derive the present-day global MFs. Additionally, the masses, mass-to-light ratios, half-mass radii and fraction of remnants have been estimated for 31 GCs with available radial velocity information.

This represents one of the largest data sets for the GC present-day MFs constraining its variation with measurements in the outer regions of GCs. The MF slopes within our sample vary in the range $-1.2 \lesssim \alpha \lesssim 0$ and are comparable with the MFs found by SB17, who estimated MFs by focusing only on the GCs central region. This work represents an improvement with respect to the work by SB17 since most GCs of their sample extend far outside the field of view of the ACS, possibly under/overestimating the degree of mass segregation (see Sollima et al. 2015). However, our result showed

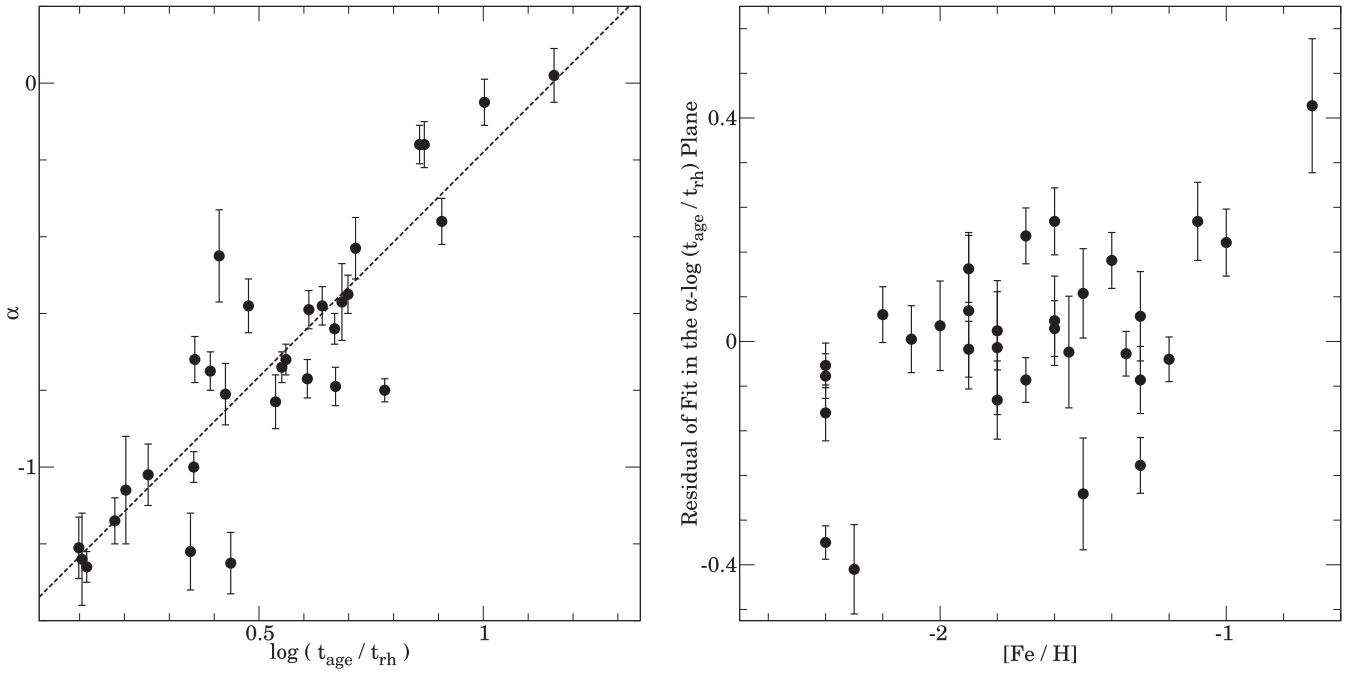

Figure 13. Left-hand panel: slope of GC MFs as a function of the ratio of lifetime to present-day half-mass relaxation time. The least-squares fit is marked by the dashed line. Right-hand panel: residual of fit in the $\alpha - \log(t_{\rm age}/t_{\rm rh})$ plane against metallicity.

that the average difference between the two works is $\Delta\alpha = 0.03$ which is even smaller than the formal errors of the MF slope for each GC. Nevertheless, we have estimated flatter MFs for a few GCs (actually the most extended of the SB17 sample).

The estimated masses and half-mass radii are in good agreement with those found by SB17 and BH18, although significant differences are apparent for some extended GCs.

By analysing the radial variation of the MF slopes for each GC, we found that King-Michie multimass models adequately reproduce the observations for most GCs, but they underestimate the degree of mass segregation in dense GCs. While we cannot exclude that this evidence is an artefact due to an overestimation of the completeness in the crowded central regions of denser GCs, this evidence could be real and indicate that GCs with denser cores evolve faster and reach a larger degree of mass segregation than what is predicted by King-Michie models. In this respect, a similar result has been found by Sollima et al. (2017) comparing various snapshots of N-body simulations selected at different stages of evolution with the same family of multimass models adopted here and found that over a long time interval, as the GC approaches the core-collapse phase, simulations reach a degree of mass segregation much larger than that indicated by the best fit analytical models.

We evaluated the present-day Jacobi radii for our GCs and estimated that, while around 60 per cent of them are tidally underfilling with $r_{\rm h}/r_{\rm J} \lesssim 0.08$, in the outer Galactic region (at $R_{GC} > 8$ kpc) two distinct groups are distinguishable: the tidally underfilling and compact GCs with mean half-mass density $\rho_{h,m} \approx 110\,{\rm M}_{\odot}{\rm pc}^{-3}$ and the tidally filling and extended GCs with $\rho_{h,m} \approx 6\,{\rm M}_{\odot}{\rm pc}^{-3}$. The GCs in the second group have small masses and are closer to dissolution. The existence of these two groups of GCs was put forward by Baumgardt et al. (2010) on the basis of a sample of half-mass and Jacobi radii calculated using single-mass fit to the projected density profile and assuming a simplified Galactic potential. They interpreted this evidence as a dichotomy in the primordial size of proto-GCs, similarly to what is observed in dwarf galaxies and young clusters in the Milky Way (Da Costa et al. 2009; Pfalzner 2009). Unfortunately, only a few GCs of our sample populate the region at large Galactocentric distances, where most of the tidally filling GCs reside in the Baumgardt et al. (2010) sample. In particular, only 3 GCs classified by Baumgardt et al. (2010) as tidally filling (NGC 288, NGC 5053, and NGC 5466) are included in our sample, two of them have $r_{\rm h}/r_{\rm J} > 0.08$.

By investigating possible correlations between various parameters, we found that MF slope correlates significantly with half-mass relaxation time as previously suggested by Paust et al. (2010), Leigh et al. (2012) and SB17. Other correlations have been found to be less significant and mainly driven by implicit correlations with $t_{\rm rh}$ (like the ones with the present-day positions of GCs in the Galaxy, $R_{\rm GC}$ and Z, claimed by Djorgovski et al. 1993; Capaccioli et al. 1993; Piotto & Zoccali 1999, and those with the average apo-/perigalactic distances). This result confirms the theoretical predictions provided by several studies (Baumgardt & Makino 2003; Gieles et al. 2011), indicating that the MF slope is controlled by two-body relaxation and evaporation across the cluster tidal boundary. In particular, two-body relaxation leads to an efficient exchange of kinetic energy between GC stars, with the less massive stars gaining orbital energy. These stars reach the border of the GC potential well and escape in a time-scale proportional to the inverse of the squared energy (Fukushige & Heggie 2000). Hence, the short relaxation time causes a fast and efficient depletion of low-mass stars in the MF (see the left-hand panel of Fig. 13).

We investigate the significance of bivariate correlations between all the possible pairs of parameters. We found that, adopting the relaxation time as a first correlator, a significant bivariate correlation is found with metallicity. This second-order correlation strongly depends on a few GCs lying at the extremes of the metallicity range covered by our sample. Its significance is therefore not clear. However, if true, this correlation would indicate a flatter MF for

more metal-rich GCs, in agreement with the predictions of star formation theories on the dependence of the IMF slope on metal content (Silk 1977; Marks et al. 2012; Chabrier et al. 2014).

We do not find any correlation between α and concentration, as claimed by de Marchi et al. (2007). Such a correlation has not been found in any of the studies based on *HST* data sets, i.e. Paust et al. (2010) and SB17.

The analysis presented here represents a further step forward in the determination of the dynamical properties of GCs, in particular their MF. While improvements on the observational side (like a better photometric coverage of the cluster extent, a larger sample of kinematics information, etc.) would be valuable to further reduce uncertainties and the possible bias, the next important improvement is likely linked to the theoretical modelling of these stellar systems. In particular, the results presented here indicate that analytical models provide only a first-order approximation of the mass segregation occurring in GCs. This might lead to significant systematics in the determined structural/dynamical quantities. Sophisticated techniques like direct *N*-body fitting (BH18) including a realistic treatment of tidal interaction, the development of velocity anisotropy and the effect of binary interactions are becoming feasible in the near future and represent the next step-forward in the determination of structural/dynamical parameters of GCs.

ACKNOWLEDGEMENTS

We warmly thank the anonymous referee for his/her helpful comments and suggestions. H. Ebrahimi thanks the Ministry of Science, Research and Technology of Iran for providing fellowship in support of this research and gratefully acknowledge support by the INAF Osservatorio di Astrofisica e Scienza dello Spazio di Bologna. We also thank Paolo Montegriffo and Barbara Lanzoni for their helpful support.

REFERENCES

Aguilar L., Hut P., Ostriker J. P., 1988, ApJ, 335, 720
Alexander P. E. R., Gieles M., Lamers H. J. G. L. M., Baumgardt H., 2014, MNRAS, 442, 1265
Anderson J. et al., 2008, AJ, 135, 2055
Bastian N., Covey K. R., Meyer M. R., 2010, ARA&A, 48, 339
Baumgardt H., Hilker M., 2018, MNRAS, 478, 1520 (BH18)
Baumgardt H., Makino J., 2003, MNRAS, 340, 227
Baumgardt H., Parmentier G., Gieles M., Vesperini E., 2010, MNRAS, 401, 1832
Baumgardt H., Hilker M., Sollima A., Bellini A., 2019, MNRAS, 482, 5138
Bergbusch P. A., VandenBerg D. A., 1992, ApJS, 81, 163
Brent R. P., 1973, Algorithm for Minimization without Derivatives. Prentice-Hall, Englewood Cliffs, NJ
Capaccioli M., Piotto G., Stiavelli M., 1993, MNRAS, 261, 819
Cappellari M. et al., 2006, MNRAS, 366, 1126
Chabrier G., 2003, PASP, 115, 763
Chabrier G., Hennebelle P., Charlot S., 2014, ApJ, 796, 75
Conroy C., van Dokkum P. G., Villaume A., 2017, ApJ, 837, 166
Czekaj M. A., Robin A. C., Figueras F., Luri X., Haywood M., 2014, A&A, 564, A102
Da Costa G. S., Grebel E. K., Jerjen H., Rejkuba M., Sharina M. E., 2009, AJ, 137, 4361
Da Rio N., Robberto M., Hillenbrand L. A., Henning T., Stassun K. G., 2012, ApJ, 748, 14
de Marchi G., Paresce F., 1995, A&A, 304, 211
de Marchi G., Paresce F., Portegies Zwart S., 2005, in Corbelli E., Palle F., Zinnecker H., eds, Astrophysics and Space Science Library, Vol. 327, The Initial Mass Function 50 years Later. Springer, Dordrecht, p. 77
de Marchi G., Paresce F., Pulone L., 2007, ApJ, 656, L65
Djorgovski S., Piotto G., Capaccioli M., 1993, AJ, 105, 2148
Dolphin A., 2016, DOLPHOT: Stellar photometry, Astrophysics Source Code Library, ascl:1608.013
Dolphin A. E., 2000, PASP, 112, 1383
Dotter A., Chaboyer B., Jevremović D., Baron E., Ferguson J. W., Sarajedini A., Anderson J., 2007, AJ, 134, 376
Dotter A. et al., 2010, ApJ, 708, 698
Frank M. J., Grebel E. K., Küpper A. H. W., 2014, MNRAS, 443, 815
Fukushige T., Heggie D. C., 2000, MNRAS, 318, 753
Gennaro M. et al., 2018, ApJ, 855, 20
Gieles M., Heggie D. C., Zhao H., 2011, MNRAS, 413, 2509
Giersz M., 2001, MNRAS, 324, 218
Giersz M., Heggie D. C., 1996, MNRAS, 279, 1037
Gunn J. E., Griffin R. F., 1979, AJ, 84, 752
Haghi H., Hoseini-Rad S. M., Zonoozi A. H., Küpper A. H. W., 2014, MNRAS, 444, 3699
Haghi H., Zonoozi A. H., Kroupa P., Sambaran B., Baumgardt H., 2015, MNRAS, 454, 3872
Harris W. E., 1996, AJ, 112, 1487
Johnston K. V., Spergel N. S., Hernquist L., 1995, ApJ, 451, 598
Joshi K. J., Nave C. P., Rasio F. A., 2001, ApJ, 550, 691
Kaliari J. S., Saul Davis D., Richer H. B., Bergeron P., Catelan B. M. S., Hansen B. M. S., Rich R. M., 2009, APJ, 705, 408
King I. R., 1966, AJ, 71, 64
Kroupa P., 2001, MNRAS, 322, 231
Kroupa P., 2002, Science, 295, 82
Kroupa P., Tout C. A., Gilmore G., 1993, MNRAS, 262, 545
Kroupa P., Weidner C., Pflamm-Altenburg J., Thies I., Dabringhausen J., Marks M., 2013, in Oswalt T. D., Gilmore G., eds, Planets, Stars and Stellar Systems, Vol. 5, The Stellar and Sub-Stellar Initial Mass Function of Simple and Composite Populations. Springer, Dordrecht, p. 115
Lamers H. J. G. L. M., Baumgardt H., Gieles M., 2013, MNRAS, 433, 1378
Leigh N., Umbreit S., Sills A., Knigge C., de Marchi G., Glebbeek E., Sarajedini A., 2012, MNRAS, 422, 1592
McLaughlin D. E., van der Marel R. P., 2005, ApJS, 161, 304
Madrid J. P., Hurley J. R., Martig M., 2014, ApJ, 784, 95
Marín-Franch A. et al., 2009, ApJ, 694, 1498
Marks M., Kroupa P., Dabringhausen J., Pawlowski M. S., 2012, MNRAS, 422, 2246
Massey P., 2003, ARA&A, 41, 15
Michie R. W., 1963, MNRAS, 125, 127
Miller G. E., Scalo J. M., 1979, ApJS, 41, 513
Milone A. P. et al., 2012, A&A, 540, A16
Milone A. P. et al., 2017, MNRAS, 464, 3636
Mor R., Robin A. C., Figueras F., Roca-Fàbrega S., Luri X., 2019, A&A, 624, L1
Moraux E., Bouvier J., Stauffer J. R., Cuillandre J.-C., 2003, A&A, 400, 891
Murphy B. W., Cohn H. N., Lugger P. M., 2011, ApJ, 732, 67
Nardiello D. et al., 2018, MNRAS, 481, 3382
Ostriker J. P., Spitzer L. Jr, Chevalier R. A., 1972, ApJ, 176, L51
Paust N. E. Q. et al., 2010, AJ, 139, 476
Pfalzner S., 2009, A&A, 498, L37
Piotto G., Zoccali M., 1999, A&A, 345, 485
Piotto G. et al., 2015, AJ, 149, 91
Robin A. C., Reylé C., Derrié S., Picaud S., 2003, A&A, 409, 523
Rybizki J., Just A., 2015, MNRAS, 447, 3880
Salpeter E. E., 1955, ApJ, 121, 161
Sarajedini A. et al., 2007, AJ, 133, 1658
Schneider F. R. N., Izzard R. G., Langer N., de Mink S. E., 2015, ApJ, 805, 20
Sheikhi N., Hasheminia M., Khalaj P., Haghi H., Zonoozi A. H., Baumgardt H., 2016, MNRAS, 457, 1028
Silk J., 1977, ApJ, 214, 718
Simioni M. et al., 2018, MNRAS, 476, 271
Sirianni M. et al., 2005, PASP, 117, 1049

Sollima A., 2019, MNRAS, 489, 2377
Sollima A., Baumgardt H., 2017, MNRAS, 471, 3668 (SB17)
Sollima A., Mastrobuono Battisti A., 2014, MNRAS, 443, 3513
Sollima A., Bellazzini M., Lee J. -W., 2012, ApJ, 755, 156
Sollima A., Baumgardt H., Zocchi A., Balbinot E., Gieles M., Hénault-Brunet V., Varri A.L., 2015, MNRAS, 451, 2185
Sollima A., Dalessandro E., Beccari G., Pallanca C., 2017, MNRAS, 464, 3871
Spitzer L. Jr, 1987, Dynamical Evolution of Globular Clusters. Princeton Univ. Press, Princeton, NJ
Takahashi K., Lee H. M., 2000, MNRAS, 316, 671
van den Bergh S., Morbey C., Pazder J., 1991, ApJ, 375, 594
van Dokkum P. G., Conroy C., Villaume A., Brodie J., Romanowsky A. J., 2017, ApJ, 841, 68
Watkins L. L., van der Marel R. P., Bellini A., Anderson J., 2015, ApJ, 803, 29
Webb J. J., Leigh N. W. C., 2015, MNRAS, 453, 3278
Webb J. J., Leigh N., Sills A., Harris W. E., Hurley J. R., 2014, MNRAS, 442, 1569
Webbink R. F., 1985, in Goodman J., Hut P., eds, Proc. IAU Symp. Vol. 113, Dynamics of Star Clusters. Kluwer, Dordrecht, p. 541
Weights D. J., Lucas P. W., Roche P. F., Pinfield D. J., Riddick F., 2009, MNRAS, 392, 817
Weisz D. R. et al., 2013, ApJ, 762, 123
Zhang Z. -Y., Romano D., Ivison R. J., Papadopoulos P. P., Matteucci F., 2018, Nature, 558, 260
Zonoozi A. H., Küpper A. H. W., Baumgardt H., Haghi H., Kroupa P., Hilker M., 2011, MNRAS, 411, 1989
Zonoozi A. H., Haghi H., Küpper A. H. W., Baumgardt H., Frank M. J., Kroupa P., 2014, MNRAS, 440, 3172
Zonoozi A. H., Haghi H., Kroupa P., Küpper A. H. W., Baumgardt H., 2017, MNRAS, 467, 758

SUPPORTING INFORMATION

Supplementary data are available at *MNRAS* online.

Figures cmd2 and cmd3: Same as Fig. 2 but for the other 30 GCs.
Figures dR1 and dR2: Same as Fig. 3 but for the other 30 GCs.

Please note: Oxford University Press is not responsible for the content or functionality of any supporting materials supplied by the authors. Any queries (other than missing material) should be directed to the corresponding author for the article.

This paper has been typeset from a TEX/LATEX file prepared by the author.